

The first hours and days of the 2021 explosion of the recurrent symbiotic nova RS Ophiuchii

AUGUSTIN SKOPAL ¹, MARTIN VRAŠŤÁK,² FRANCOIS TEYSSIER ³, MITSUGU FUJII,⁴ SERGEI SHUGAROV ¹,
MIROSLAV ŠLECHTA ⁵ AND MAREK WOLF ⁶

¹*Astronomical Institute, Slovak Academy of Sciences, 059 60 Tatranská Lomnica, Slovakia*

²*Private observatory Liptovská Štiavnica, Kľúčiny 457/74, Slovakia*

³*ARAS Eruptive Stars Group, F-76100 Rouen, France*

⁴*Fujii Kurosaki Observatory, 4500 Kurosaki, Tamashima, Kurashiki, Okayama 713-8126, Japan*

⁵*Astronomical Institute, Czech Academy of Sciences, 251 65, Ondřejov, Czech Republic*

⁶*Astronomical Institute of Charles University, V Holešovičkách 2, 180 00, Praha 8, Czech Republic*

ABSTRACT

The accretion of matter on a massive white dwarf (WD) can lead to repeated nuclear explosions on its surface over a timescale of years to decades. The seventh explosion of the recurrent symbiotic nova RS Ophiuchi (RS Oph) was recorded on August 8, 2021. In this paper, we examine its early evolution, from 9 hours before its optical maximum until day 42. We achieved our goal by modeling the spectral energy distribution (SED) using optical spectroscopy and simultaneous BVR_CI_C photometry, supplemented by $JHKL$ photometry and ultraviolet spectroscopy from previous explosions in 2006 and 1985. Our SED models revealed an early stage of development of the ejecta bipolar structure, consisting of a flared, density-enhanced equatorial disk and low-density regions in bipolar directions. The comparability of the internal shocks' luminosity in the equatorial outflow, inferred from our model parameters, with the luminosity of the warm WD pseudophotosphere during its presence in the spectrum (until \sim day 42) confirmed that a significant part of its radiation originates from reprocessed shock emission. We explain the formation and evolution of the bipolar ejecta structure during RS Oph explosions by the rotation of the accreting WD. Such an ejecta structure provides a natural framework for the generation of strong internal shocks and thus γ -ray emission inside the ejecta.

Keywords: High energy astrophysics (739) — Cataclysmic variable stars (203) — Symbiotic binary stars (1674)— Recurrent novae (1366)

1. INTRODUCTION

A nonmagnetic white dwarf (WD) accreting from a main-sequence star in cataclysmic variables (CVs) or from an evolved giant in symbiotic stars (SySts) can accumulate hydrogen-rich matter until its pressure and temperature at the WD surface reach critical values at which thermonuclear runaway (TNR) is triggered, causing an optical brightening up to ~ 15 mag. We observe the classical nova (CN; in CVs) or symbiotic nova (SyN; in SySts) explosion (e.g., Bode & Evans 2008; Starfield et al. 2016; Munari 2025, for a review). If mass is accreted onto a massive WD ($>1 M_\odot$), an explosive TNR under degenerate conditions due to strong surface gravity will ignite, and form a very fast nova. If in this case, accretion proceeds at a high rate of several

times ($10^{-8} - 10^{-7}$) $M_\odot \text{ yr}^{-1}$, the TNR will repeat on a timescale of human life. These events are called recurrent (symbiotic) novae (e.g., Yaron et al. 2005).

RS Ophiuchi (RS Oph) is a recurrent SyN whose explosions are characterized with an optical brightening by ~ 7 mag and an average recurrence period of ~ 15 years (Schaefer 2010). The most recent explosion was reported on August 8, 2021 (see vsnet-alert 26131⁷). The binary of RS Oph consists of a massive WD accreting from the wind of a K7 III – M2 III red giant (RG) in a 453.6-d orbit (Mürset & Schmid 1999; Pavlenko et al. 2008; Brandi et al. 2009; Zamanov et al. 2018). The mass ratio of the binary components, $M_{\text{RG}}/M_{\text{WD}} = 0.56$, and

⁷ <http://ooruri.kusastro.kyoto-u.ac.jp/mailarchive/vsnet-alert/26131>.

the assumed WD mass of $1.2\text{--}1.4 M_{\odot}$, correspond to the orbital inclination of $49^{\circ}\text{--}52^{\circ}$ (Brandi et al. 2009).

The attractiveness of the recurrent novae phenomenon has led to the use of available observational techniques to obtain observations in the widest possible energy range, as well as spatial imaging of the explosion remnants. Radio observations of the 1985 explosion, thus first detected the non-spherical shape of the nova ejecta (Taylor et al. 1989), which was later confirmed and refined for the 2006 (e.g., O’Brien et al. 2006; Rupen et al. 2008) and the 2021 eruption (Munari et al. 2022; de Ruiter et al. 2023; Lico et al. 2024). The latter studies on the 2021 outburst showed that the bipolar structure of the radio emission is remarkably similar to that from the 2006 outburst, with a density enhancement in the orbital plane that obscures the receding emission lobe (Munari et al. 2022). In particular, for the ejecta of the 2006 outburst, the bipolar shaping was also indicated by the interferometric technique in the near- and mid-IR (e.g., Chesneau et al. 2007; Barry et al. 2008), by the *HST* imaging in the optical (Bode et al. 2007), and by the *Chandra* X-ray Observatory (Luna et al. 2009). Later, in 2009 and 2011, the *Chandra* X-ray images detected the east–west extended emission with opening angles of $\approx 70^{\circ}$, consistent with a picture of sharply slowing equatorial flow but fast bipolar outflow (Montez et al. 2022). Such shaping was recently supported by the discovery of a prolonged ($\sim 16 \times 5$ pc) super-remnant cavity surrounding RS Oph formed by sweeping up local interstellar medium by the nova eruptions over its lifetime (Healy-Kalesh et al. 2024). Also, the spectropolarimetric monitoring of the 2021 eruption revealed the presence of dust between days 2 and 9, the spatial distribution of which was asymmetric, with components both aligned with and perpendicular to the orbital plane of the binary (Nikolov et al. 2023). Since the early dust was present at about the same time when both the optical brightness and γ -ray emission detected by Fermi-LAT peaked (see Fig. 2 of Cheung et al. 2022), the spectropolarimetric measurements supported the link between shocks and dust in RS Oph (see Nikolov et al. 2023).

The 2021 outburst of RS Oph was intensively observed in the γ -ray energies, using Fermi-LAT ($0.1\text{--}23$ GeV, Cheung et al. 2022; Zheng et al. 2022), H.E.S.S. (100 GeV – 2 TeV, H. E. S. S. Collaboration et al. 2022), MAGIC ($60\text{--}250$ GeV, Acciari et al. 2022), and LST-1 ($\sim(40\text{--}700)$ GeV, Abe et al. 2025). To explain the very-high-energy (VHE; 100 GeV $< E < 100$ TeV) and high-energy (HE; 100 MeV $< E < 100$ GeV) γ -ray emission, a hadronic scenario of particle acceleration in the nova shock was preferred over an alternative leptonic scenario in these studies. However, modeling the HE–

VHE spectral energy distribution (SED) during 4 days after the outburst, De Sarkar et al. (2023) showed that the VHE γ -ray data can be explained by a hadronic component, whereas the HE data satisfy rather a leptonic component. The SED model was consistent with radio low-frequency data. Diesing et al. (2023) demonstrated that, contrary to previous studies, a single shock cannot simultaneously explain the observed γ -ray spectrum of RS Oph. Instead, they proposed a model involving multiple shocks that reproduces the GeV to TeV spectrum and its temporal evolution. The model is supported by the presence of multiple distinct velocity components in the optical spectrum during the first few days of the explosion (see Munari & Valisa 2021; Tomov et al. 2023). By modeling X-ray observations of RS Oph obtained with NICER ($0.2\text{--}12$ keV), Islam et al. (2024) found evidence of the interaction of the ejecta with dense equatorial matter during the initial phase, and with less dense matter in the polar regions in the later phases of the outburst, which is consistent with the shaping of the ejecta suggested by radio and γ -ray observations. Similar to other powerful γ -ray novae, RS Oph shows a correlation between optical and γ -ray light curves (LCs; Cheung et al. 2022), suggesting that a significant portion of the energy of the internal shocks is converted into optical light around its maximum (see Metzger et al. 2014; Li et al. 2017; Aydi et al. 2020).

Multifrequency observations of the last three RS Oph explosions (1985, 2006, and 2021) revealed their striking similarity. For the 2006 and 1985 eruptions, Rosino (1987), Banerjee et al. (2009), and Ness et al. (2007) pointed out the similarity of the LC profiles in the optical, near-IR, and supersoft X-ray regions. The similarity of the 2021 eruption to the previous one in 2006 has also been noted in several studies, mostly as a side result (e.g., Acciari et al. 2022; Munari et al. 2022; Azzollini et al. 2023). However, the supersoft X-ray source (SSS) emission of the 2021 explosion was found to be weaker and switched off earlier than in the 2006 explosion (Page et al. 2022; Orío et al. 2023). Analyzing the X-ray grating spectra of both the 2006 and 2021 outbursts, Ness et al. (2023) explained the lower SSS emission observed in 2021 by a higher absorption from cold (neutral) and hot (ionised) material in the line of sight.

In this study, we analyze the optical continuum emitted by the material ejected during the 2021 RS Oph explosion, with the primary goal of determining the evolution of its physical parameters and fundamental structure from 14 hours after the start of brightening to the supersoft X-ray source phase (\approx day 40). We also analyze the evolution of the H α line, which helps us un-

derstand the properties of the ejecta, and, in particular, the surrounding environment it penetrates.

Our analysis and its results are described in Sect. 3, their discussion and connections with the results obtained from other spectral domains are given in Sect. 4, whereas Sect. 5 provides a summary of our results.

2. OBSERVATIONS

2.1. Photometry

For the purpose of this work, we used multicolor BVR_{CI} photometry collected by members of the American Association of Variable Star Observers (AAVSO)⁸, by members of the Variable Star Observers League in Japan (VSOLJ), Itoh, Kiyota, Moriyama, Sano, and Sato as collected by Hiroyuki Maehara⁹, and those published by Acciari et al. (2022).

Further $UBVR_{CI}$ photometry was carried out using the *FLI ML3041* CCD camera (2048×2048 px, pixel size: 15 μm × 15 μm, scale: 0.4 arcsec/px, FoV: 14′ × 14′), mounted at the Cassegrain focus of the 60 cm, f/12.5 telescope, operated by the Astronomical Institute of the Slovak Academy of Sciences. The data were reduced using the *IRAF* software package¹⁰ as described by Parimucha & Vaňko (2005). Corresponding magnitudes (Table 4) were obtained using the comparison stars listed in Table 1 of Sekeráš et al. (2019).

Multicolor photometry was primarily used to scale the relative flux units of the low-resolution spectra (Table 6) to absolute units and to verify the calibration of the high-resolution spectra (Table 7), which were used for modeling the SED (see Appendix B).

2.2. Spectroscopy

In this work, we primarily use ground-based optical spectroscopy. Most of the spectra were obtained by amateurs within the initiative *Astronomical Ring for Access to Spectroscopy* (ARAS), which promotes cooperation between professional and amateur astronomers in the field of spectroscopy¹¹. The spectra containing the Balmer jump, obtained by one of us (MV), were crucial for our work. The amateurs spectra were taken at 18 different observatories and/or private stations. Basic information about their spectral acquisition equipment is introduced in Table 1. The list of spectra with low ($R = 500 - 1300$) and medium resolution ($R = 8,500 - 20,000$) is in Table 6 and 8.

At the Ondřejov Observatory, medium-resolution spectra ($R \sim 13,000$) covering the red spectral region were secured at the coudé focus of the 2.0 m reflector (see Skoda et al. 2002). Standard initial reduction (bias subtraction, flat-fielding, creation of 1D spectra, and wavelength calibration) was performed using modified *IRAF* packages. The times and spectral ranges of individual observations are listed in Table 8, where they are labeled by 'Ondrejov'.

Furthermore, we used high-resolution spectra downloaded from the European Southern Observatory (ESO) Science Archive Facility with DOI: <https://doi.org/10.18727/archive/50>. The spectra were obtained using the high-resolution echelle spectrograph UVES (see Dekker et al. 2000) attached to the Nasmyth B focus of the UT2 Kueyen telescope at the ESO Paranal Observatory (see Molaro et al. 2023). They cover the spectrum from ~ 304 to ~ 946 nm and have a resolution power from $\sim 58,640$ to $\sim 107,200$. The list of the used UVES spectra is given in Table 7. They are labeled as 'Paranal' in Table 9.

The low-resolution spectra (Table 6), preferentially those covering the Balmer discontinuity, as well as the high-resolution UVES spectra, after an appropriate reduction of their resolution, were primarily used to model their SED (Sect. 3.2). Their flux calibration was verified with the aid of the (near-)simultaneous (U) BVR_{CI} photometry (see Appendix B). Medium- and high-resolution spectra served to analyze variations in the line profiles and fluxes (Figs. 7, and 8, 8, and 13, Table 9). Absolute fluxes of their used parts were obtained with the aid of the two neighboring SED models (see Fig. 11).

The strong similarity of the RS Oph outbursts (see Sect. 1) allows us to consider observations obtained at the same time after the optical maximum of different outbursts as simultaneous. Therefore, we also used ultraviolet (UV) spectra made with the *International Ultraviolet Explorer* (*IUE*) taken during the 1985 outburst and the near-infrared (near-IR) *JHKL* photometry obtained during the 1985 and 2006 outbursts, published by Evans et al. (1988), West (2006), and Banerjee et al. (2009). These observations confirmed the strong similarity between RS Oph outbursts in the UV to near-IR and, conversely, verified the correctness of our optical SED models (see Sect. 3.2.2, Fig. 4).

Observations were dereddened with $E_{B-V} = 0.69$ (Zamanov et al. 2018) using the extinction curve of Cardelli et al. (1989) and the distance-dependent parameters were scaled to a canonical value of 1.6 kpc (Hjellming et al. 1986).

⁸ <https://www.aavso.org/databases>

⁹ <http://kws.cetus-net.org/~maehara/LCG.html>

¹⁰ <http://iraf.noao.edu>

¹¹ <https://aras-database.github.io/database/>

Table 1. Log of observatories and instruments used to obtain amateur spectroscopic observations.

Observatory	Telescope [†]	Spectrograph	Camera	Resolution [‡]	Observer	Reference	Label*
OSJ-CA ^(a)	37	Alpy 600	ATIK 414EX	1,000	Desrosiers	2	(i)
FKO ^(b)	40	FBSPEC-IV	ASI6200MM-PRO	500	Fujii	1,4	(ii)
WCO-UK ^(c)	28	LISA	SXVR-H694	1,000	Boyd	1,2	(iv)
KOL-SK ^(d)	28	LISA	ATIK 460EX	680	Dubovský	3,2	(iii)
THO-UK ^(e)	28	Alpy 600	ATIK 428	1,000	Leadbeater	2	(vi)
LSO ^(f)	36	UVEX	ATIK 414EX	870	Vrašťák	2	(vii)
LSO ^(f)	36	FEST	QHY 294M-PRO	13,500	Vrašťák	2	(vii)
SMM-SP ^(g)	40	B60050-VI	ATIK 460EX	9,500	Teyssier	1,2	(xiii)
SMM-SP ^(g)	40	B60050-VI	ASI 2600MM	8,500	Guarro	1,2	(x)
DUR-FR ^(h)	51	echelle	ATIK 460EX	11,000	Charbonnel	2,4	(xi)
ARM-AU ⁽ⁱ⁾	25	LISA	ATIK 314L	16,000	Bohlsen	2,4	(xiv)
OCT-FR ^(j)	18	Lhires3 2400	ATIK 460EX	18,700	Boussin	2	(xv)
AQL-IT ^(k)	22	Lhires3 2400	ST 8300	13,100	Sollecchia	2	(xx)
AQL-IT ^(k)	22	Lhires 600	SXVR-H694	3,900	Berardi	2	(xviii)
UNM-US ^(l)	35	Lhires3 2400	ATIK 460EX	20,000	Doctor	2	(xix)
HOR-UK ^(m)	35	Lhires3 2400	ATIK 460EX	18,500	Martin	2	(xxi)
ANT-FR ⁽ⁿ⁾	20	SOLEX500	ASI 183MM	1,300	Buil	2	(v)
ANT-FR ⁽ⁿ⁾	20	SOLEX2400	ASI 183MM	16,700	Buil	2	(xvi)
ORL-FR ^(o)	25	Alpy 600	ATIK 414EX	600	Lecocq	2	(viii)
OBE-FR ^(p)	31	echelle	ATIK 460EX	11,000	Thizy	2	(ix)
OTO-FR ^(q)	40	echelle	ATIK 460EX	11,000	Garde	1,2	(xii)
MAR-AU ^(r)	100	eShel	ATIK 460EX	10,000	Eldridge	2	(xvii)

Notes. ^(a) Mont St-Joseph Observatory, ^(b) Fujii Kurosaki Observatory, ^(c) West Challow Observatory, ^(d) Astronomical Observatory at the Kolonica Saddle, ^(e) Three Hills Observatory, ^(f) Liptovská Štiavnica Observatory, ^(g) Santa Maria de Montmagastrell Observatory, ^(h) Durtal Observatory, ⁽ⁱ⁾ Mirranook Observatory, ^(j) Observatory de l'Eridan, ^(k) L'Aquila Bellavista Observatory, ^(l) private station in Las Cruces, New Mexico, ^(m) Huggins Observatory, Rayleigh, ⁽ⁿ⁾ Antibes, ^(o) Orlienas, ^(p) Observatoire de la Belle Etoile, ^(q) Observatoire de la Tourbière, ^(r) Mardella.

[†] Diameter of the primary mirror in cm, [‡] average resolution, * label of the observatory in Tables 6, 8, and 9.

References. 1 – Skopal et al. (2017), 2 – Teyssier (2019), 3 – Kudzej & Dubovský (2014), 4 – Skopal et al. (2014).

3. ANALYSIS AND RESULTS

3.1. Times of maxima and onsets of the last 3 explosions

Figure 1 compares the V and visual LCs around the brightness maximum of the RS Oph explosion in 1985, 2006, and 2021. The time of the maximum brightness, t_{\max} , could only be determined for the 2021 explosion, which was observed both before and after the maximum. By fitting 131 V magnitudes around the maximum with a polynomial of the third degree, we determined t_{\max} of the 2021 eruption at JD 2,459,435.96 \pm 0.06 (August 9.46 \pm 0.06, 2021). The last observation in quiescence (11.7, no filter) was made on August 8.49, 2021, by the VSOLJ observer Tadashi Kojima (vsnet-alert 26136). This date and the first date, when RS Oph was indicated in outburst (August 8.53, 2021; $V = 9.10\pm 0.032$),

allowed us to estimate the time of the start of the optical brightening, t_0 , at JD 2,459,435.01 \pm 0.02 (August 8.51 \pm 0.02, 2021), 0.95 \pm 0.08 days before the time t_{\max} .

The 2006 explosion was captured right at its visual maximum of 4.5 mag by Narumi et al. (2006) on February 12.83, 2006. A previous observation on February 11.86, indicated a quiescent phase of RS Oph at visual magnitude 11.0 (see AAVSO database), 0.97 days before the peak brightness. The onset and the peak brightness of the 2006 explosion coincide with the timing of the 2021 explosion within its uncertainties (see Fig. 1). Therefore, for the 2006 explosion, we adopted the same uncertainties in t_0 and t_{\max} times.

The first visual magnitudes of the 1985 explosion, 6.8 and 5.2, were estimated by Morrison (1985) in January 1985 26.47 and 28.45, respectively. Based on the similarity of the LCs of all three explosions, shifting the

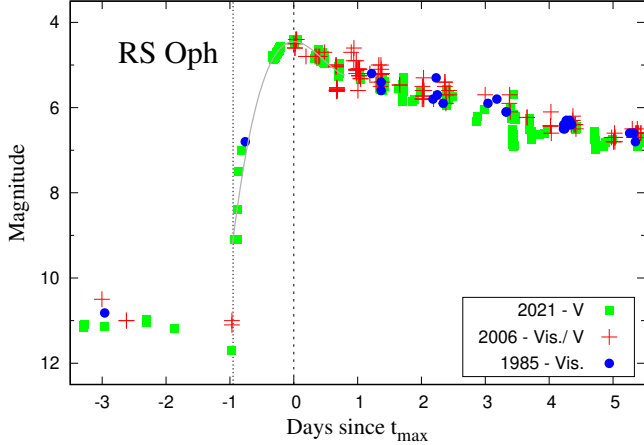


Figure 1. Comparison of V and visual LCs of RS Oph around the maxima of its explosions in 2021, 2006, and 1985. The gray curve is a third-degree polynomial that fits the V magnitudes around the 2021 maximum. The vertical dotted and dashed lines indicate the time of the brightness onset and its maximum, respectively (Table 2, Sect. 3.1).

1985 LC to match the LC profiles of the 2006 and 2021 explosions showed that the first magnitude is located before the maximum, while the second one is placed after it (see Fig. 1)¹². This allowed us to estimate the t_{\max} time of the 1985 explosion at January 27.23±0.12 (JD 2,446,092.73±0.12), where the uncertainty is the sum of the uncertainties in the t_{\max} times of the explosions in 2006 and 2021, i.e., 0.12 d. For time t_0 we adopted the same error as we estimated for the 2006 and 2021 eruptions. Table 2 summarizes t_{\max} and t_0 times for the 1985, 2006, and 2021 RS Oph explosions.

Finally, the time elapsed after time t_{\max} is called the nova age, unless otherwise stated.

3.2. Modeling the SED

In this section, using the method of disentangling composite spectra of symbiotic stars (see Skopal 2005), we determine the basic physical parameters of the WD pseudophotosphere (WDP) along the outburst, from our first observations on day -0.366 to the beginning of the SSS phase (\sim day 40). The presence of emission lines in the spectrum from the very beginning of the explosion, especially prominent H I lines of the Balmer series (e.g., Taguchi et al. 2021; Munari & Valisa 2021), and the Balmer jump in emission (see Appendix C) reflect the presence of a nebular continuum in the spectrum. Therefore, we assume that the spectrum of the ejecta consists of two main components of radiation: The stel-

¹² We omitted the estimate from January 27.20 (6.2 mag) because it was more than 1.5 mag below the predicted values.

Table 2. Times of brightening onset, t_0 , and maximum, t_{\max} , for the RS Oph explosions in 2021, 2006, and 1985 (see Sect. 3.1).

Outburst	t_0	t_{\max}
	Date (UT)	Date (UT)
	JD ₀ 2,4...	JD _{max} 2,4...
	Orbital phase ^(a)	Orbital phase
2021	August 8.51±0.02	August 9.46±0.06
	59,435.01±0.02	59,435.96±0.06
	0.727	0.729
2006	February 11.86±0.02	February 12.83±0.06
	53,778.36±0.02	53,779.33±0.06
	0.257	0.259
1985	January 26.27±0.02	January 27.23±0.12
	46,091.77±0.02	46,092.73±0.12
	0.311	0.313

Notes. ^(a) According to the ephemeris of the inferior conjunction of the RG, $T_{\text{conj.}} = \text{JD } 2,445,043.54 + 453.6 \times E$ (Brandi et al. 2009).

lar component(s) from the WDP(s), and the nebular continuum emitted by the hydrogen plasma.

In the early stages of nova evolution, the radiation from the WDP often dominates the optical and resembles the spectra of A to F-type stars (e.g., Warner 2008). Here we refer to it as a *warm* WDP. In later phases, usually when the nebular radiation starts to be more pronounced in the spectrum, the radiation from the warm WDP is better approximated by a blackbody radiation (see Fig. 3 here or Fig. 13 of Pandey et al. 2025).

A relative strong nebular component of radiation in the spectrum signals the presence of a hot ionizing source in the system – a *hot* WDP, because the warm WDP is unable to generate the observed amount of nebular emission (see Sect. 4.1).

The radiation of the warm and hot WDP is described and modeled in Sects. 3.2.1 and 3.2.2. Their geometrical structure within the ejecta is suggested in Sect. 4.1 and sketched in Fig. 2.

3.2.1. Parameters of the warm WD pseudophotosphere and the nebula

According to the predicted components of the radiation from the RS Oph ejecta, similar to the case of CN V339 Del SED modeling (see Sect. 3.1. of Skopal et al. 2014), the reddening-free continuum of the RS Oph ejecta measured at Earth, can be written in the form,

$$F(\lambda) = \theta_{\text{WD}}^2 \mathcal{F}_\lambda(T_{\text{eff}}) + k_{\text{N}} \times \varepsilon_\lambda(H, T_e), \quad (1)$$

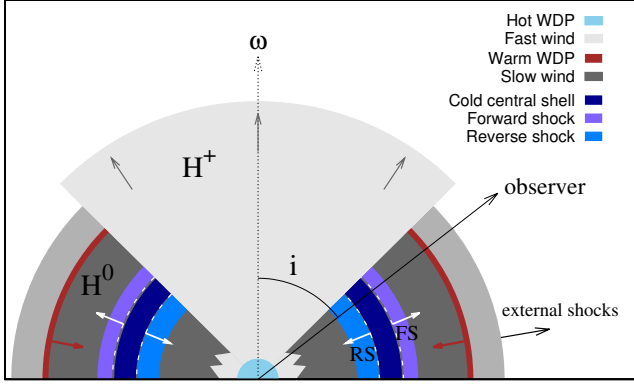


Figure 2. Sketch for the RS Oph ejecta inferred from SED models (side view, Sect. 4.1). Due to the WD rotation, the wind is compressed and slowed down towards the equator at the expense of the polar directions, where we indicate a fast ionized wind (Sect. 4.2). The radius of the optically thick/thin compressed wind interface (i.e., the warm WDP, brown line) starts to shrink after the maximum due to its expansion and the lowering of \dot{M}_{WD} (brown arrow, see Table 3). The earliest optically thin wind above the warm WDP (medium gray band) shocks the surrounding much less dense and relatively stable giant wind. Structure of the internal shocks in the slow dense outflow was adapted according to Fig. 1 of Metzger et al. (2015). White arrows indicate the propagation of forward (FS) and reverse (RS) shocks. H^0 and H^+ denote the neutral and ionized parts of the ejecta, and i is the orbital inclination. The axis of rotation (ω) is shown by the dotted arrow.

or

$$F(\lambda) = \theta_{\text{WD}}^2 \pi B_{\lambda}(T_{\text{BB}}) + k_{\text{N}} \times \varepsilon_{\lambda}(\text{H}, T_{\text{e}}), \quad (2)$$

where the first term at the right represents the stellar component of radiation from the warm WDP compared to a synthetic spectrum $\mathcal{F}_{\lambda}(T_{\text{eff}})$ (Eq. (1)) or to a blackbody radiation (Eq. (2)), calculated for the temperature T_{eff} or T_{BB} , respectively. Their scaling to the measured spectrum, the angular radius of the WDP, $\theta_{\text{WD}} = R_{\text{WD}}^{\text{eff}}/d$ is given by its effective radius $R_{\text{WD}}^{\text{eff}}$ (which is the radius of a sphere with the same luminosity) and the distance d . The second term at the right is the nebular continuum expressed by its volume emission coefficient, $\varepsilon_{\lambda}(\text{H}, T_{\text{e}})$ ($\text{erg cm}^3 \text{s}^{-1} \text{\AA}^{-1}$), scaled with the factor $k_{\text{N}} = EM/4\pi d^2$, where EM (cm^{-3}) is the emission measure given by the proton and electron concentration within a volume of the ionized hydrogen. The electron temperature T_{e} and thus $\varepsilon_{\lambda}(\text{H}, T_{\text{e}})$ are assumed to be constant throughout the nebula¹³. For the

¹³ This assumption is justified by the fact that elastic collisions between free electrons occur on a significantly shorter timescale than their inelastic collisions with other atoms or ions in the plasma, which leads to the rapid thermalization of electrons

sake of simplicity, we considered only contributions from f–b and f–f transitions in hydrogen plasma.

In modeling the SED, we compared a grid of models given by Eq. (1) or (2) with the observed spectrum. The grid of synthetic spectra was prepared using the library of Munari et al. (2005) for $T_{\text{eff}} = 5,000 - 15,000$ K with a step of 250 K, and fixed other atmospheric parameters ($\log(g) = 2.5$, $[\text{M}/\text{H}] = 0$, $[\alpha/\text{Fe}] = 0$, $v_{\text{rot}} = 20 \text{ km s}^{-1}$, and microturbulent velocity = 2 km s^{-1})¹⁴. For the spectra covering the Balmer discontinuity, we estimated the continuum fluxes by eye, adopted their uncertainty at 5%, and selected the model corresponding to a minimum of the reduced χ^2 function. In the remaining cases, when the Balmer jump region is not available, we first estimated T_{e} with the aid of models of the neighboring spectra covering this region¹⁵. Second, we adjusted the other parameters (k_{N} , θ_{WD} , $T_{\text{eff}}/T_{\text{BB}}$) and, based on our experience, we selected the one whose model matched the observed continuum. In this way we determined the model parameters, θ_{WD} , T_{WD} (i.e., T_{eff} or T_{BB}), k_{N} , and T_{e} that correspond to the luminosity of the warm WDP, $L_{\text{WD}}^{\text{warm}} = 4\pi d^2 \theta_{\text{WD}}^2 \sigma T_{\text{WD}}^4$, $R_{\text{WD}}^{\text{eff}} = d \theta_{\text{WD}}$, and $EM = 4\pi d^2 k_{\text{N}}$ of the nebular continuum (see Table 3, Fig. 3). Finally, the radiation from the giant was adopted according to Skopal (2015). However, its contribution in the spectrum was negligible, at least, until \sim day 30 (see Fig. 4).

We note that the warm WDP dominated the spectrum only around the brightness maximum. From day -0.366 to day $+0.130$, its effective radius increased from ~ 114 to $\sim 290 R_{\odot}$, and cooled from $\sim 11,000$ to $\sim 7,250$ K, respectively. Before the maximum, the nebular spectrum was indicated only by hydrogen emission lines. Its continuum could not be extracted because it was relatively faint, and our spectrum did not contain the Balmer jump region. The nebular continuum was first unambiguously determined by the UVES spectrum on day 0.617 (see Fig. 3 d).

3.2.2. Parameters of the hot WD pseudophotosphere

The original radiation of the hot WDP was first measured with IUE on day 6.6 after the peak of the 1985 outburst. This component dominates the far-UV (see Fig. 4 d – i), but it is very weak in the optical – seen as a faint Rayleigh-Jeans tail of a hot blackbody radiation (see Fig. 3 i – l). We considered its contribution from

and, hence, a Maxwellian velocity distribution (Bohm & Aller 1947).

¹⁴ The fixed parameters mainly affect the spectral line profile, while T_{eff} mainly determines the continuum profile.

¹⁵ Note that T_{e} determines the height of the Balmer jump and the slope of the nebular continuum.

Table 3. Physical parameters of the nova RS Oph from the first hours of its life.

Age ^a JD-JD _{max}	Warm WD pseudophotosphere			Hot WD pseudophotosphere			Nebula		
	$T_{\text{eff}}/T_{\text{BB}}$ (kK)	$R_{\text{WD}}^{\text{eff}}$ (R_{\odot})	$L_{\text{WD}}^{\text{warm}}$ ($10^{37} \text{ erg s}^{-1}$)	$T_{\text{BB}}^{\text{ion}}$ (kK)	$R_{\text{WD}}^{\text{eff}}$ (R_{\odot})	$L_{\text{WD}}^{\text{hot}}$ ($10^{39} \text{ erg s}^{-1}$)	T_e (kK)	EM (10^{62} cm^{-3})	\dot{M}_{WD} ($10^{-4} M_{\odot} \text{ yr}^{-1}$)
-0.366	11.0±0.5 ^b	114±6	65±6	–	–	–	–	–	–
0.130	7.25±0.25 ^b	290±14	80±8	73 ^d	3.7	>1.4	≈15	≥1.5	~2.29
0.348	7.15±0.15 ^b	258±13	60±7	73 ^d	4.8	>2.3	~16	~2.6	~3.47
0.478	7.00±0.20 ^b	251±13	52±6	73 ^d	5.0	>2.4	~18	~3.1	~3.85
0.617	7.00±0.20 ^b	201±11	34±5	73 ^d	6.3	>3.9	18.0±2	4.90±0.30	5.50
1.006	7.00±0.20 ^b	179±9	27±4	73 ^d	6.1	>3.6	19.0±2	4.90±0.35	5.36
1.409	7.00±0.20 ^b	164±9	22±3	73 ^d	5.2	>2.7	19.0±2	3.67±0.27	4.47
1.567	7.00±0.20 ^b	161±9	22±3	73 ^d	5.0	>2.4	19.5±2	3.32±0.24	4.15
2.391	7.20±0.20 ^c	144±8	19±2	73 ^d	4.8	>2.3	19.0±2	3.10±0.21	3.99
3.395	7.50±0.30 ^c	105±5	12±2	73 ^d	4.6	>2.1	16.0±2	2.40±0.20	3.31
3.759	5.20±0.30 ^c	190±10	9.1±1.0	73 ^d	3.7	>1.4	26.0±2	2.42±0.20	3.03
4.751	4.60±0.20 ^c	206±10	6.6±1.0	73 ^d	3.6	>1.3	26.0±2	2.25±0.20	2.88
5.416	4.40±0.20 ^c	196±10	5.0±0.7	~86 ^e	~2.5	~1.2	25.0±2	1.96±0.20	2.13
5.759	4.10±0.30 ^c	223±13	4.8±0.7	~89 ^e	~2.2	~1.1	26.0±2	1.84±0.20	2.02
7.343	3.70±0.20 ^c	230±12	3.4±0.6	~84 ^e	~2.4	~0.99	18.0±2	1.23±0.15	1.61
9.510	3.90±0.30 ^c	183±12	2.7±0.5	~80 ^e	~2.2	~0.67	19.5±2	0.92±0.11	1.41
11.048	3.70±0.20 ^c	179±10	2.1±0.4	~84 ^e	~1.9	~0.62	22.0±2	0.89±0.09	1.18
11.559	3.80±0.20 ^c	160±10	1.8±0.4	~92 ^e	~1.6	~0.65	20.0±2	0.89±0.09	1.16
12.421	3.80±0.20 ^c	183±10	2.4±0.4	~72 ^e	~2.2	~0.45	22.0±2	0.68±0.09	1.11
15.998	3.80±0.20 ^c	139±8	1.4±0.2	~90 ^f	~1.6	~0.57	20.0±2	0.58±0.08	0.863
19.989	3.60±0.20 ^c	121±7	0.85±0.2	~117 ^f	~1.1	~0.80	19.0±2	0.40±0.05	0.587
21.583	3.80±0.20 ^c	105±6	0.80±0.2	~134 ^f	~0.94	~0.98	21.0±2	0.41±0.05	0.563
25.356	~3.00 ^c	~85	~0.20	~144 ^f	~0.90	~1.2	18.0±2	0.34±0.04	0.498
26.559	3.20±0.18 ^c	113±6	0.46±0.1	~153 ^f	~0.75	~1.1	23.0±2	0.28±0.04	0.425
31.349	–	–	–	~157 ^f	~0.63	~0.84	20.0±2	0.29±0.03	0.378
32.549	3.60±0.20 ^c	59±4	0.20±0.05	~153 ^f	~0.56	~0.59	25.0±2	0.21±0.03	0.319
33.361	–	–	–	~155 ^f	~0.63	~0.79	20.0±2	0.21±0.03	0.329
37.532	3.60±0.20 ^c	40±4	0.09±0.03	~155 ^f	~0.39	~0.30	25.0±2	0.14±0.02	0.221
42.566	3.60±0.20 ^c	39±4	0.09±0.03	~162 ^f	~0.37	~0.32	27.0±2	0.11±0.015	0.180

Notes:

^a JD_{max} = 2 459 435.96 (2021 August 9.46) is the date of the optical maximum in *V* (Table 2). ^b T_{eff} , ^c T_{BB} , ^d adopted value, ^e *Zanstra*-temperature, ^f from He II $\lambda 4686/\text{H}\beta$ flux ratio (see Sect. 3.2.2 for determining the temperature $T_{\text{BB}}^{\text{ion}}$).

day 5.416, when this component began to be identifiable in the vicinity of the Balmer jump (see Fig. 3i). We adjusted its radiation using the far-UV fluxes of the nearest *IUE* spectrum scaled to the short-wavelength part of the modeled optical spectrum. It slightly reduced the height of the Balmer jump, which required a slightly higher T_e .

Assuming that the nebular continuum grows from complete absorption of hydrogen ionizing photons emitted by the hot WDP, we can determine its fundamental

parameters, $L_{\text{WD}}^{\text{hot}}$, $R_{\text{WD}}^{\text{eff}}$, and temperature, $T_{\text{BB}}^{\text{ion}}$. From day 5.416, when the flux of the hot WDP can be estimated from the far-UV, $T_{\text{BB}}^{\text{ion}}$ can be approximated by the temperature of a blackbody radiation that is just capable of producing the observed EM when scaled to far-UV fluxes – the so-called *Zanstra*-temperature. According to Skopal (2015), $T_{\text{BB}}^{\text{ion}}$ can be obtained by solving the equation

$$\frac{k_{\text{N}}}{F_{\text{WD}}(\lambda)} \alpha_{\text{B}}(\text{H}, T_e) \pi B_{\lambda}(T_{\text{BB}}^{\text{ion}}) - f(T_{\text{BB}}^{\text{ion}}) = 0, \quad (3)$$

where the flux of the ionizing source, $F_{\text{WD}}(\lambda)$, is selected at a wavelength λ , at which it dominates the spectrum (in the far-UV), $\alpha_{\text{B}}(\text{H}, T_{\text{e}})$ is the total recombination coefficient to all but the ground state of hydrogen ($\text{cm}^3 \text{s}^{-1}$), and the function $f(T_{\text{BB}}^{\text{ion}})$ determines the flux of ionizing photons emitted by 1 cm^2 area of the blackbody source ($\text{cm}^{-2} \text{s}^{-1}$). Solution of Eq. (3) for the values of k_{N} , $F_{\text{WD}}(\lambda)$, λ and $\alpha_{\text{B}}(\text{H}, T_{\text{e}})$ provides $T_{\text{BB}}^{\text{ion}}$. Having $T_{\text{BB}}^{\text{ion}}$, we can estimate the $L_{\text{WD}}^{\text{hot}}$ of the hot WDP as (see e.g., Skopal et al. 2017),

$$L_{\text{WD}} = \alpha_{\text{B}}(\text{H}, T_{\text{e}}) EM \frac{\sigma T_{\text{BB}}^{\text{ion}4}}{f(T_{\text{BB}}^{\text{ion}})}, \quad (4)$$

and $R_{\text{WD}}^{\text{eff}}$ is given by the Stefan–Boltzmann law.

From the beginning of the eruption to day 4.751, when the hot WDP was not directly identifiable in the spectrum, we adopted $T_{\text{BB}}^{\text{ion}} = 73,000 \text{ K}$, at which the source generates maximum flux of hydrogen ionizing photons for a given luminosity. In other words, this temperature determines the minimum of the function (4) that, when scaled with the measured EM , provides the lower limit of $L_{\text{WD}}^{\text{hot}}$ (see Fig. A.1. of Skopal 2015).

From \sim day 16, when the emission of the recombination $\text{He II } \lambda 4686$ line appeared in the spectrum, we estimated $T_{\text{BB}}^{\text{ion}}$ from the $\text{He II } \lambda 4686/\text{H}\beta$ flux ratio (e.g., Gurzadyan 1997). We used the approach of Skopal et al. (2020) for the average $T_{\text{e}} = 22,000 \text{ K}$ during this period (see their Eq. (6)).

Parameters of the hot WDP, $T_{\text{BB}}^{\text{ion}}$, $R_{\text{WD}}^{\text{eff}}$, and $L_{\text{WD}}^{\text{hot}}$ are introduced in Table 3. Their temporal evolution is depicted in Fig. 5 and examples of SED models are shown in Figs. 3 and 4.

3.2.3. Plausibility of the hot WDP parameters

The parameters $L_{\text{WD}}^{\text{hot}}$, $R_{\text{WD}}^{\text{eff}}$ and $T_{\text{BB}}^{\text{ion}}$ of the hot WDP, determined in the manner described in Sect. 3.2.2, represent only estimates of their actual values. The assumption of ionization equilibrium is probably fulfilled only in the initial phase of the outburst, when the maximum EM is observed. However, the lack of knowledge of the exact value of $T_{\text{BB}}^{\text{ion}}$ during this period allows only a lower limit of the $L_{\text{WD}}^{\text{hot}}$ to be determined. In the later phase of nova evolution (\gtrsim days 5), $T_{\text{BB}}^{\text{ion}}$ can be determined more accurately, as *Zanstra*-temperature. However, ionization equilibrium may not be achieved, as indicated by a marked decrease in EM . In this case, a part of ionizing photons is not absorbed in the nebula, leading to a decrease in EM that corresponds to a lower $L_{\text{WD}}^{\text{hot}}$ than the real one (see Eq. (4)).

Consistent with the bipolar structure of the ejecta (see Sect. 4.1), the hot WDP will probably not be spherically symmetric with a non-spherical temperature dis-

tribution – hotter regions with smaller radii are located at/around its poles and cooler regions with larger radii are located toward the WD equator (see Sect. 4.2.1 of Skopal 2019, for comparison with CN V339 Del). However, viewing the hot WDP from a single polar angle (the orbital inclination), we can determine only one $T_{\text{BB}}^{\text{ion}}$ for which we determine the scaling (i.e., $R_{\text{WD}}^{\text{eff}}$) and $L_{\text{WD}}^{\text{hot}}$ assuming spherical symmetry, which is not true. This is probably the main source of systematic errors in determining the parameters of the hot WDP.

3.3. Mass-loss rate by the ionized ejecta

At the very beginning of a nova outburst, the optically thick wind occurs deep inside the WD photosphere, extinguishing the X-ray flash by strong absorption (e.g., Kato & Hachisu 1994; Kato et al. 2022). From a certain point in a nova evolution, the wind is ionized by the radiation from the hot WDP, converting it into the nebular radiation via f–f and f–b transitions. Knowing the result of these processes, i.e., EM of the nebular continuum and/or the flux in the line (e.g., in $\text{H}\alpha$), we can determine the mass and mass-loss rate of the ionized ejecta as a function of the nova age. In determining these parameters, we will assume a biconical structure of the ejecta, in which the ionized part is distributed symmetrically in the polar regions, determined by the opening angle from the polar axis (see Sect. 4.1, Fig. 2).

In our case, the nebular component of radiation was measurable already from the maximum of the optical brightness (day 0.130, Table 3, Fig. 3). According to the relationship between EM and \dot{M}_{WD} (see Eq. (C.5) of Skopal et al. 2017), derived for a spherically symmetric, β -law wind of Lamers & Cassinelli (1999), the mass-loss rate can be expressed as

$$\dot{M}_{\text{WD}}(EM) = \mu m_{\text{H}} v_{\infty} [f 4\pi EM b R_0 (1 - 2\beta) B^{-1}]^{1/2}, \quad (5)$$

where

$$B = \left[\left(1 - \frac{bR_0}{R_{\text{neb}}}\right)^{1-2\beta} - \left(1 - \frac{bR_0}{R_{\text{WD}}^{\text{eff}}}\right)^{1-2\beta} \right]. \quad (6)$$

The parameter f is the fractional solid angle that bounds the ionized part of the ejecta around the polar axis, μ is the mean molecular weight, and m_{H} is the mass of the hydrogen atom. The wind starts at the radial distance, R_0 , from the WD center with the initial velocity a , and it is accelerated with the factor β to the terminal velocity, v_{∞} . It becomes optically thin at the radius of the hot WDP, $R_{\text{WD}}^{\text{eff}}$, and it reaches the outer radius of the ionized ejecta, R_{neb} , at the given time of the observation. The parameter $b = 1 - (a/v_{\infty})^{1/\beta}$.

In determining \dot{M}_{WD} from the very beginning of the 2021 RS Oph eruption, we used parameters of the SED

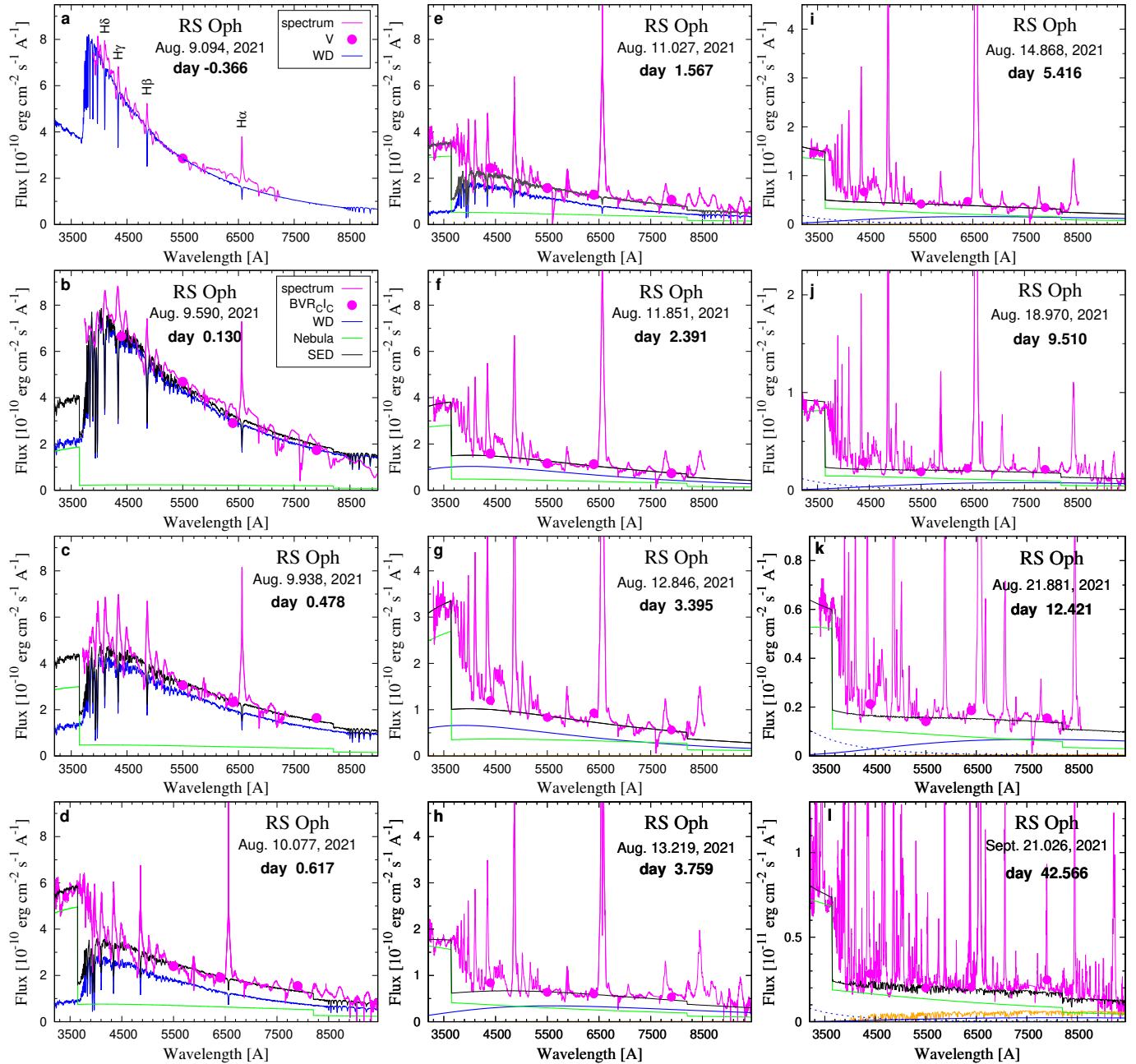


Figure 3. Examples of the observed (in magenta) and modeled (black lines) SEDs of RS Oph at selected dates from the onset of its 2021 outburst. The meaning of lines and symbols is as shown in the keys (top left panels). The solid blue line represents the radiation of the warm WDP, while the dotted blue line (from day 5.416) represents the radiation of the hot WDP (see Sect. 3.2). The spectrum of the giant (in orange, panel l) was taken from Skopal (2015), recalculated for $E_{B-V} = 0.69$.

models, EM and $R_{\text{WD}}^{\text{eff}}$ (Table 3), v_{∞} from the extension of $H\alpha$ wings (Table 9), $\beta = 0.56$ as suggested by fitting the broad $H\alpha$ profile just after the 2006 eruption (see Skopal et al. 2008), and $a = 50 \text{ km s}^{-1}$ (Skopal et al. 2017)¹⁶. The outer radius $R_{\text{neb}} = R_{290} v_{\infty} \Delta t$, where,

R_{290} is the radius of the warm WDP on day 0.130, when the nebular component was first detected, and Δt is the time between day 0.130 and a later observation. Since the actual beginning of the wind is not further specified, we adopted two limiting values for R_0 : $R_0 = R_{\text{WD}}^{\text{eff}}$ that

¹⁶ Due to the very fast wind acceleration, the high value of v_{∞} , and its uncertain beginning inside the photosphere, the value

of a between ~ 10 and $\sim 100 \text{ km s}^{-1}$ affects the resulting \dot{M}_{WD} within a few percents only

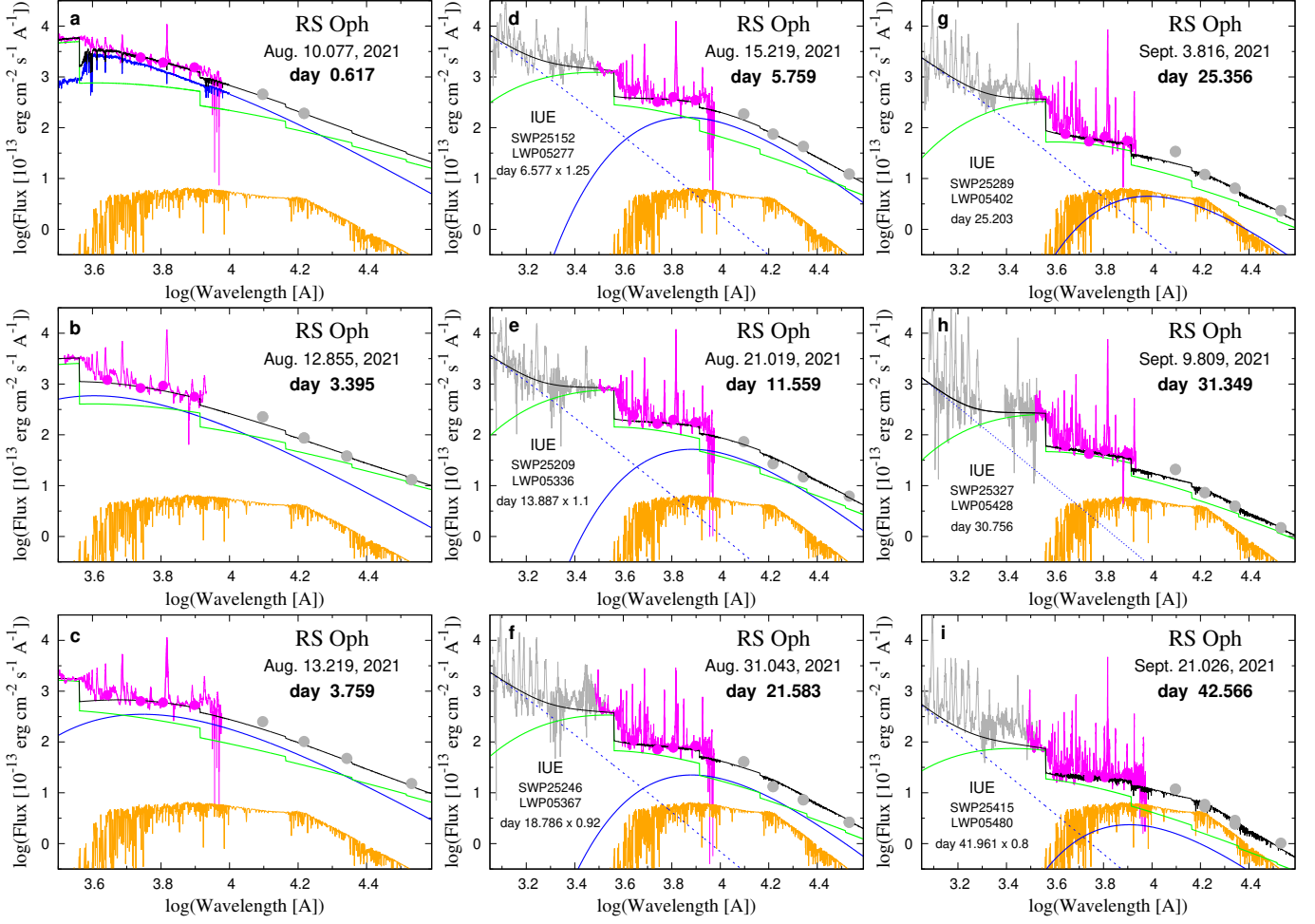


Figure 4. Examples of SED models in the UV/optical/near-IR domain. Given the similarity of the RS Oph eruptions, our observations were supplemented with (near-)simultaneous observations of the previous two eruptions (in gray). Denotation of lines and points is the same as in Fig. 3.

corresponds to the lower limit of \dot{M}_{WD} and R_0 equals the WD core radius of $0.004 R_{\odot}$ (for a WD mass of $\sim 1.3 M_{\odot}$, see Nauenberg 1972), which provides the upper limit of \dot{M}_{WD} . Table 3 presents the average of these limits, while Fig. 6 a also shows its maximum deviations. As the limits of R_0 are not physically possible, the actual uncertainties of \dot{M}_{WD} are smaller than the figure shows.

As the nebular continuum and emission lines (e.g., of hydrogen) arise in the same ionized volume, the value of \dot{M}_{WD} can also be determined from the measured flux of the $\text{H}\alpha$ broad component, F_{α} , produced by the ionized part of the ejecta. Its luminosity, $L_{\alpha} = 4\pi d^2 F_{\alpha}$, is related to the line emissivity, $\varepsilon_{\alpha} n_e n_p$ ($\text{erg cm}^{-3} \text{s}^{-1}$), by

$$L_{\alpha} = \varepsilon_{\alpha} \int_V n_e n_p dV = \varepsilon_{\alpha} EM, \quad (7)$$

where ε_{α} is the volume emission coefficient in $\text{H}\alpha$, n_e and n_p are concentrations of electrons and protons, and V is the volume of the ionized part of the wind. Accord-

ingly, using the same assumptions as for the continuum, Eq. (5) can be rewritten as

$$\dot{M}_{\text{WD}}(\text{H}\alpha) = \mu m_{\text{H}} v_{\infty} \left[f \frac{4\pi}{\varepsilon_{\alpha}} L_{\alpha} b R_0 (1 - 2\beta) B^{-1} \right]^{1/2}. \quad (8)$$

However, in a line transition, the wind becomes optically thin at distances $> R_{\text{WD}}^{\text{eff}}$. Leitherer (1988) found that winds of O stars become optically thin in the $\text{H}\alpha$ line from a distance of ~ 1.5 times the star's radius. Also, modeling of the broad $\text{H}\alpha$ wings in the spectra of symbiotic stars suggested the optically thin conditions from about 1.2 to 1.5 $R_{\text{WD}}^{\text{eff}}$ (Skopal 2006). In the expression B of Eq. (5), we assume the optically thin wind in the $\text{H}\alpha$ line from a radius of $1.2 R_{\text{WD}}^{\text{eff}}$. Using our values of F_{α} (Table 9), radii of the hot WDP in Table 3 interpolated to dates of high- and medium-resolution spectra containing the $\text{H}\alpha$ line, and $\varepsilon_{\alpha} = 1.83 \times 10^{-25} \text{ erg s}^{-1} \text{ cm}^3$ (Osterbrock 1989) for our average T_e of 20,000 K (see

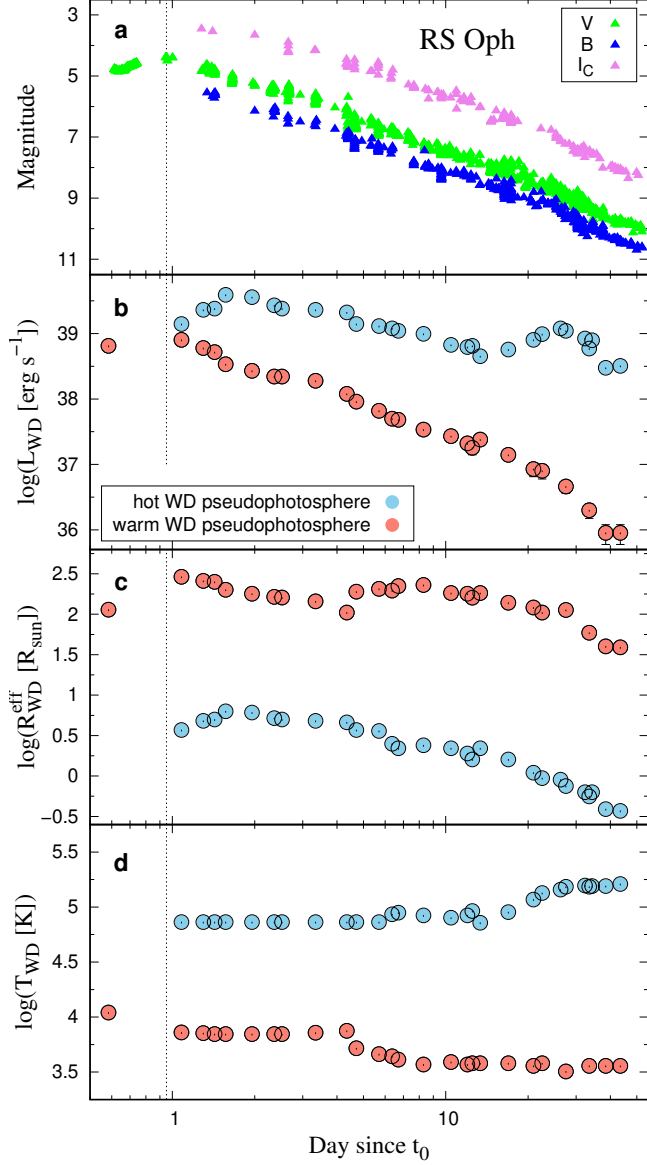


Figure 5. The B , V , and I_C LCs (panel (a)), and evolution in L_{WD} (b), $R_{\text{WD}}^{\text{eff}}$ (c), and T_{WD} (d) parameters from the onset of the RS Oph explosion, t_0 . Parameter values are in Table 3. The dotted line indicates the time of the optical maximum.

Table 3), we obtained the corresponding \dot{M}_{WD} (Fig. 6 a, Table 9).

The values of \dot{M}_{WD} determined in this way suffer from systematic errors. For example, it is the unknown value of the factor f at a given observation time. For simplicity, we have used $f = 1$. The uncertain determination of the hot WDP parameters (see Sect. 3.2.3) represents another source of errors that cannot be specified. For example, a small jump in \dot{M}_{WD} from the $\text{H}\alpha$ flux since \sim day 15 (Fig. 6 a) could be related to the increase in $T_{\text{BB}}^{\text{ion}}$ when the $\text{He II } \lambda 4686$ emission appeared in the spectrum.

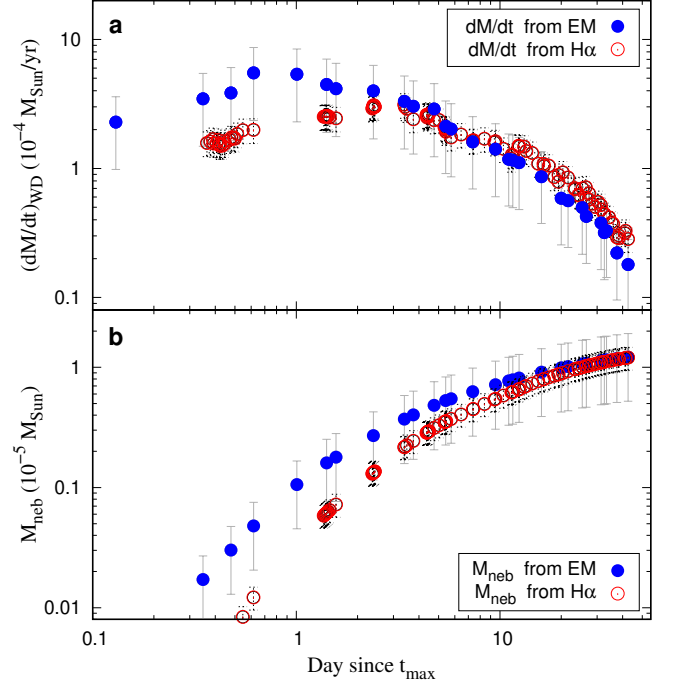


Figure 6. Mass-loss rate by the ionized part of the ejecta, \dot{M}_{WD} (panel (a)), and its corresponding mass, M_{neb} (b). See Sects. 3.3 and 3.4.

However, its reality is not supported by the \dot{M}_{WD} values determined from EM .

3.4. Mass released by the ionized ejecta

The mass of the ionized part of the ejecta can be estimated by integrating its outflow rate from the first detection of the nebular continuum on day 0.13 to our last SED model on day 42.6, i.e.

$$M_{\text{neb}} = \int_{0.13}^{42.6} \dot{M}_{\text{WD}} dt. \quad (9)$$

Figure 6 b shows the increase in M_{neb} from the peak brightness to day 43, when its mean value was $1.2 \times 10^{-5} M_{\odot}$. This value can be considered final, as the decrease in EM as well as $\text{H}\alpha$ flux after \approx day 33 (see Tables 3 and 9) indicates a decrease in the wind mass-loss rate, which is consistent with the onset of the SSS phase in the nova evolution (see Ness et al. 2023). According to theoretical considerations by Hachisu & Kato (2010), the emergence of supersoft X-rays indicates that the optically thick wind has stopped or substantially weakened and therefore the total mass of the ejecta remains constant in time. However, our value of M_{neb} represents rather a lower limit, because a part of the ejected mass at the very beginning of the eruption was not ionized.

Assuming $T_e = 10^4$ K, Molaro et al. (2023) determined the ejected mass to be $2.9 \times 10^{-5} (d/2.4 \text{ kpc}) M_{\odot}$

from the $H\beta$ flux measured at the beginning of the nebular phase. This value is ~ 1.6 times higher than our value and represents an upper limit, since the $H\beta$ emission includes a contribution from the ionized wind from the giant, measured during quiescence. Therefore, [Molaro et al. \(2023\)](#) also used a flux of $\text{He II } \lambda 4686$, which corresponded to an ejected mass of $1.1 \times 10^{-5} (d/2.4 \text{ kpc}) M_{\odot}$ which is ~ 1.6 times lower than our value, $1.2 \times 10^{-5} (d/1.6 \text{ kpc}) M_{\odot}$. The authors noted that the uncertainty in T_e , 2,000 K, corresponds to changes in M_{neb} by a factor of ~ 2 , being higher at higher T_e , and vice versa. For comparison, $T_e \equiv 10^4 \text{ K}$ (i.e., $\varepsilon_{\alpha} = 3.56 \times 10^{-25} \text{ erg s}^{-1} \text{ cm}^3$, [Osterbrock 1989](#)) would reduce our value of M_{neb} to $8.6 \times 10^{-6} (d/1.6 \text{ kpc}) M_{\odot}$.

3.5. Evolution of the $H\alpha$ line

[Munari & Valisa \(2021, 2022\)](#) showed the detailed evolution of the $H\alpha$ line profile from the maximum of the RS Oph outburst to its nebular phase. An example of such evolution in our spectra is shown in [Fig. 13](#) (Appendix D), while [Fig. 8](#) compares the $H\alpha$ line profile at the beginning (day 1.6) and at the end (day 37.5) of optical brightening. Its typical feature is a broad emission component, triangular in profile, with FWZI of $\sim 8,000 \text{ km s}^{-1}$, and a blueward-shifted absorption component at $\sim -4,500 \text{ km s}^{-1}$, which was indicated until day 3–4. Narrow absorption and emission components are superimposed on the top of the broad component at ~ -73 and $\sim -12 \text{ km s}^{-1}$, respectively, well measurable until day 5–6, but still distinguishable until the end of our observations. Their early evolution is shown in [Fig. 8](#).

3.5.1. The broad component

The development of the $H\alpha$ broad component parameters is shown in [Fig. 7](#). The flux of its emission F_{α} ([Fig. 7 a](#)) was gradually increasing from our first observation on day 0.36, reached a maximum of $\sim 5.5 \times 10^{-8} \text{ erg s}^{-1} \text{ cm}^{-2}$ between day 3 and 6, and then was decreasing to values of $\lesssim 1 \times 10^{-8} \text{ erg s}^{-1} \text{ cm}^{-2}$ on day 42. It is natural to assume that the broad $H\alpha$ component is emitted by the ionized wind ejected from the WD during the explosion. The outflowing wind increases the particle density of the ionized medium ($n \propto \dot{M}_{\text{WD}}$), which leads to an increase in its emissivity ($\propto n^2$). At the same time, the expansion of the ionized wind reduces its density with v_{∞}^{-3} , which lengthens the recombination time ($\propto 1/n$), thereby reducing the total emission per unit time. The measured flux, which is given by the rate of recombinations, then results mostly from the rivalry of these physical processes. During the first ~ 5 days, the high value of \dot{M}_{WD} ([Fig. 6 a](#)) and a relatively small volume of the ionized ejecta result in a gradual increase of both the F_{α} flux and the height of

the broad component above the continuum, F_{max} (see [Fig. 7 a](#) and [b](#)). Furthermore, an increase in the visible volume of the biconical ionized wind due to the increase in its opening angle (see [Sect. 4.1](#)) may also contribute to the increase of both the parameters during this early evolution of the ejecta. In later stages of the nova evolution, the decreasing value of \dot{M}_{WD} and the continued wind expansion led to a marked decrease in the particle density, reducing the contributions at all wavelengths of the line. We measured a decline in all parameters (see [Figs. 7 a, b, c, and 8](#)). [Figures 7 d](#) and [8](#) show that the deceleration of the ejecta in the direction towards the observer is small (see [Sect. 4.6.2](#)).

We estimated the uncertainties of the broad component parameters as follows. The uncertainty of its flux is primarily determined by the estimate of the local continuum, which is influenced mainly by the $\text{He I } \lambda 6678$ emission. We estimated its errors to be less than 10%. We note that the $H\alpha$ emission in the UVES spectra was saturated by day 5.76, even for the shortest exposure times. Its values are therefore below by $\gtrsim 10\%$ (see panel [a](#)). Similar error values apply for the maximum height above the local continuum, while for the FWHM, the error estimate is roughly half. The terminal velocity values of the broad component are affected by the blend of a faint but broad $\text{Fe II } \lambda 6456$ and $\text{He I } \lambda 6678$ emission lines on the blue and red sides of the extended $H\alpha$ wing. We estimated their errors to be 5–10%.

Finally, the high-velocity absorption component may be associated with the neutral wind from the giant, which is swept off and shocked by the ejecta, and accumulated at its front ([O'Brien et al. 2006](#), [Sect. 4.6.2](#) here). This material absorbs the light from the underlying warm WDP in a given line transition, which is best seen in the hydrogen lines. However, its presence is limited to the first 3–4 days only when the warm WDP dominates the spectrum (see [Figs. 3](#) and [9](#)). Such behavior is related to the temporal evolution of the ejecta (see [Sect. 4.3](#)).

Further absorption/emission continues in the undisturbed wind from the giant, which is responsible for the formation of the narrow components (see [Sects. 3.5.2](#) and [4.5](#)).

3.5.2. The narrow component

A pair of narrow absorption and emission lines, located on the top of the broad emission, is observed from the very beginning of the eruptions of SyNe ([Munari 2025](#)). The case of RS Oph was recently shown in detail by [Munari & Valisa \(2021\)](#). According to the small FWHM of $\approx 20 \text{ km s}^{-1}$, their origin was ascribed to the

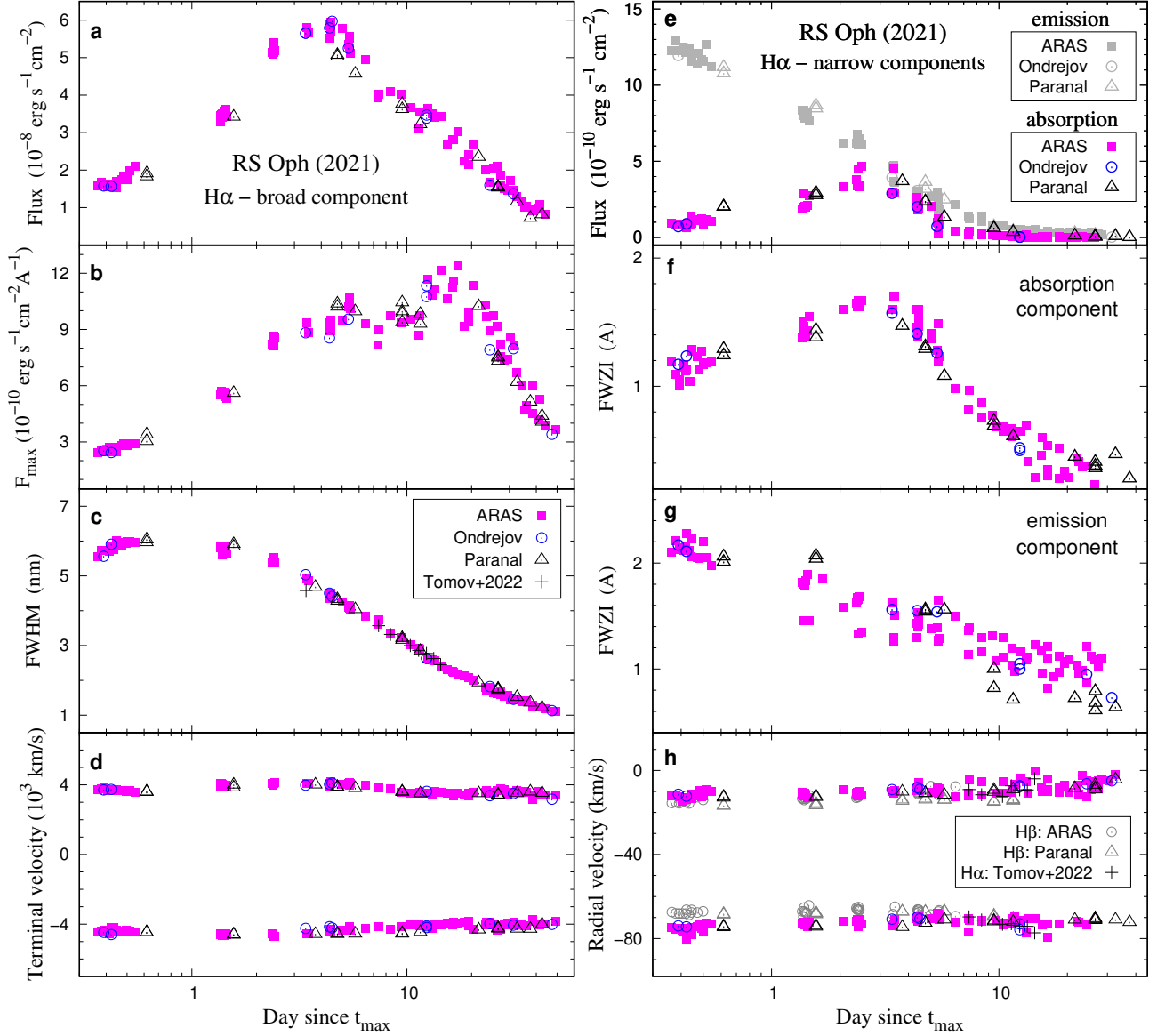


Figure 7. Evolution of the $H\alpha$ line parameters. Left: The broad component: The flux (panel (a)), its maximum height, F_{\max} , above the continuum (b), FWHM (c), and terminal velocities of the wings (d). The description is in Sect. 3.5.1 and the data in Table 9. Right: The narrow components: The fluxes (e), FWZI of the absorption (f) and emission (g) component, and their radial velocities (h). Their description and interpretation are found in Sects. 3.5.2 and 4.5, respectively.

wind from the giant surrounding the binary that is not perturbed by the ejecta (e.g., Munari 2019).

Here, Fig. 7 (panels e–h) shows the evolution of the narrow components parameters in $H\alpha$ for the recent 2021 RS Oph explosion. Panel (e) shows that the flux of the emission component decreases rapidly from a maximum of around $1.3 \times 10^{-9} \text{ erg s}^{-1} \text{ cm}^{-2}$ measured on our first spectra (day 0.36) to $<10^{-10} \text{ erg s}^{-1} \text{ cm}^{-2}$ on day $\gtrsim 10$, while the flux absorbed by the narrow component gradually increases from an initial value of $\sim 10^{-10} \text{ erg s}^{-1} \text{ cm}^{-2}$ to a value of $\sim 4 \times 10^{-10} \text{ erg s}^{-1} \text{ cm}^{-2}$ on \sim day 4, with a subsequent

decline to values $<10^{-10} \text{ erg s}^{-1} \text{ cm}^{-2}$ during days 4–6. Thereafter, very low flux values of both components were observed until our last observations. A similar course was also observed in the evolution of the width of both components; here, characterized with FWZI for simplicity (see panels (f) and (g)). Finally, panel (h) shows their RVs. The relatively stable value of the absorption component in the $H\alpha$ line, $-73 \pm 3 \text{ km s}^{-1}$, corresponds to the terminal velocity of the RG wind $34 \pm 3 \text{ km s}^{-1}$ after subtracting the systemic velocity of -39 km s^{-1} (Brandi et al. 2009). Interestingly, the RV of the $H\beta$ absorption core was shifted by $\sim 7 \text{ km s}^{-1}$ com-

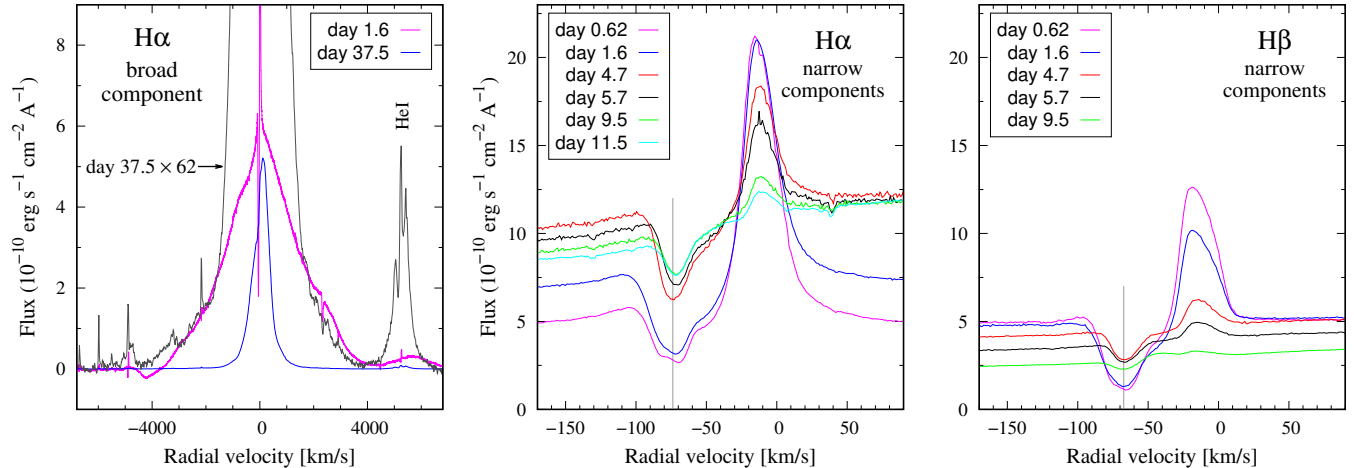


Figure 8. Example of the evolution of the broad and narrow components of the hydrogen line profiles measured on UVES spectra. Left panel shows the H α broad component measured on days 1.567 and 37.532. This comparison shows a significant narrowing of the line emission core (see Fig. 7 c), although the expansive, weak line wings remain present even in the later stage of nova evolution. The local continuum is subtracted (see Sect 3.5.1). Right panels show the evolution of the narrow components in the H α and H β profiles. Note that the transition from the emission to the absorption component is not smooth, so the resulting profile is not exactly of the P Cygni type. The vertical gray lines indicate the position of the absorption component in the H α and H β profiles, which differ by $\sim 7 \text{ km s}^{-1}$ during the first days after t_{max} (see Fig. 7 h and Sect. 3.5.2).

pared to the values for the H α core during the first ~ 5 –6 days (gray symbols in Fig. 7 h). This shift is likely due to the formation of the narrow H β absorption deeper in the absorbing column, i.e., closer to the warm WDP, where smaller RVs of the RG wind are expected compared to larger distances above the WDP, where absorption in H α arises (see Fig. 1 of Booth et al. 2016). Later, from \sim day 5.4, the RVs of H α and H β become equal, probably due to the reduced size of the undisturbed column of the wind located at larger distances from the binary (see Sect. 4.5). As concerns the narrow emission component, it is placed at $(-12 \pm 3) \text{ km s}^{-1}$ during the first ~ 4 days with a slow increasing trend to $(-8 \pm 4) \text{ km s}^{-1}$ and significantly reduced flux during the following days (see also Fig. 8). Further properties of the narrow components are described and interpreted in Sect. 4.5.

We estimated the uncertainties of the measured parameters as follows. By day ~ 5 , flux uncertainties were as small as $\sim 5\%$, as the narrow line profiles were well-defined. Later, as these components weakened, their errors increased to more than $\sim 10\%$. A similar trend in errors is estimated for the FWZI. However, in later stages (day $\gtrsim 9$), the FWZI estimate suffers from significant errors ($\gtrsim 50\%$) due to the superposition of narrow lines with the broad component, the profile of which is not precisely known. The intrinsic uncertainties in the RVs of the narrow components were relatively small, ranging from 1 to 2 km s^{-1} , but were affected by systematic errors arising from inaccurate wavelength calibration in some amateur spectra. Also, RVs measured in amateur

spectra do not include a correction for Earth’s rotation, which causes an error of $< 0.5 \text{ km s}^{-1}$.

Finally, Fig. 8 shows the evolution of the profiles of narrow components in the H α and H β lines during the first days of the explosion in very high-resolution UVES spectra. As can be seen, the emission and absorption components do not represent exactly the components of the P-Cygni profile. The two components are separated, in contrast to what can be seen in medium-resolution spectra (see Zamanov et al. 2022; Munari & Valisa 2021). The profile of the narrow components, which is not of the P Cyg type, suggests that the wind from the giant is not spherically symmetric around the binary, being diluted on the polar sides (see Sect. 4.5).

4. DISCUSSION

4.1. Bipolar density structure of the ejecta

Our SED models showed that the spectrum of the ejecta from the very beginning of the RS Oph explosion consists of a relatively cool stellar component (i.e., the warm WDP) and nebular component of radiation, the contributions of which change during the explosion (Sect. 3.2.1, Figs. 3 and 5).

For the interpretation of such a two-component spectrum, it is essential to know whether the warm WDP is capable of producing the measured amount of nebular emission. If not, there must be a strong ionizing source inside the ejecta. The spectrum of RS Oph has this feature from the very beginning of the explosion until the end of the detection of the cold stellar com-

ponent. For example, on day 0.617, the warm WDP ($L_{\text{WD}}^{\text{warm}} = 3.4 \times 10^{38} \text{ erg s}^{-1}$, $T_{\text{eff}} = 7,000 \text{ K}$) generates only $\sim 5 \times 10^{42}$ hydrogen ionizing photons per second (assuming blackbody radiation), while the measured EM of $4.9 \times 10^{62} \text{ cm}^{-3}$ is generated by $\alpha_{\text{B}}(\text{H}, T_e) \times EM = 7.8 \times 10^{49}$ recombinations per second for the total hydrogen recombination coefficient for the Case B, $\alpha_{\text{B}}(\text{H}, 18,000 \text{ K}) = 1.6 \times 10^{-13} \text{ cm}^3 \text{ s}^{-1}$ (e.g., Nussbaumer & Vogel 1987). The very low flux of ionizing photons produced by the warm WDP, which is several orders of magnitude lower than the required rate of recombinations, thus signals the presence of a strong ionizing source in the ejecta, which we have called the hot WDP (see Sect. 3.2, Fig. 2). A spectrum that arises from the superposition of the stellar and nebular components of radiation, where the former is unable to give rise to the latter, is called a spectrum of the 'two-temperature type'. It was first detected during Z And-type outbursts of SySts with high orbital inclinations (see Sect. 5.3.4 of Skopal 2005), but has also been found for CN V339 Del (see Sect. 4.2 of Skopal et al. 2014).

The two-temperature-type of spectrum can be produced by an optically thick equatorial disk-like structure of the outflowing wind (the ejecta) surrounding the burning WD, whose flared outer rim (the warm WDP) occults the central ionizing source (the hot WDP) in the line of sight, while the optically thin parts of the ejecta above/below the disk structure are ionized, giving rise to the strong nebular emission (see Fig. 27 of Skopal (2005), or Fig. 4 of Skopal (2015) for RS Oph, and Fig. 2 here). This means that the density is not uniformly distributed in the ejecta, suggesting that an optically thin, low-density parts are located in bipolar directions above the flared density-enhanced disk-like structure around the equator, which is thought to coincide with the orbital plane.

This interpretation is consistent with the bipolar shaping of the RS Oph ejecta suggested in previous studies using various techniques and observations from γ -ray to radio (see references in Sect. 1). The development of the two-temperature type spectrum from the very beginning of the RS Oph eruption suggests an equally early development of the bipolar structure of the ejecta. This is supported, for example, by the modeling of the X-ray spectrum monitored by NICER (see Islam et al. 2024) and/or spectropolarimetric observations that revealed a similarly asymmetric dust structure (Nikolov et al. 2023), in both cases, measured as early as two days after the start of the eruption. Such a structure of the nova ejecta is probably responsible for the generation of multiple shocks within the ejecta, which produce the

observed complex γ -ray spectrum (Diesing et al. 2023, Sect. 4.6 here).

4.2. Possible cause of the ejecta bipolar structure

It is thought that the formation of a bipolar density structure in classical nova ejecta may be caused by the orbital motion of the WD companion in the dense ejecta during a lengthy (weeks to months) 'common-envelope' phase. The donor experiences frictional forces in the nova envelope and transfers orbital energy and angular momentum to the ejecta, producing a 'density contrast' in the ejected mass between the polar and equatorial (orbital) directions, with concentrated mass in the latter (see Livio et al. 1990; Lloyd et al. 1997). However, for long-period symbiotic novae, this mechanism cannot be effective because the timescale of the bipolar structure formation represents only a small fraction of the orbital period. Moreover, the photospheric radius of the ejecta is smaller than the separation between the binary components – the 'common-envelope' phase does not even exist. Therefore, for symbiotic novae, we favor rapid WD rotation as the primary mechanism creating the bipolar density structure of their ejecta.

According to Bjorkman & Cassinelli (1993), the equatorial density-enhanced structure may be the result of the rotation of the star with a radiatively driven wind, which leads to compression of the outflowing material towards the equatorial regions at the expense of the polar regions due to the conservation of angular momentum of the wind particles (see Lamers & Cassinelli 1999, for a review). Cariková & Skopal (2012) applied the wind compression model to accreting WDs in symbiotic binaries during the Z And-type outbursts. In their model, the wind begins at the surface of the rotating WD and becomes optically thin at/above the hot WDP. According to the model, the wind creates a denser neutral disk-like zone in the equatorial plane, the optically thick outer edge of which represents the warm WDP, while the remaining, less dense parts of the wind above/below the disk are ionized by the hot WDP (see their Fig. 6, and compare Fig. 2 here). Such a biconical ionization structure of the ejecta can then produce the two-temperature type of spectrum as described in Sect. 4.1. The model was applied to the RS Oph eruption in 2006 (Sect. 4.1) and we therefore adopt it for its recent explosion in 2021.

The rotation of the accreting WD may therefore be responsible for the formation of the density-enhanced equatorial region and the density-reduced polar regions during their thermonuclear outbursts, when the mass-loss rate is significantly enhanced. Furthermore, due to centrifugal force, a rotating WD requires the accretion of more material to trigger a TNR, which can result in

a higher luminosity and a larger amount of ejected mass than in the case of a non-rotating WD.

4.3. Evolution of the ejecta structure

According to the wind compression model (Sect. 4.2), the formation of a dense, optically thick equatorial region of the ejecta depends mainly on the mass-loss rate, \dot{M}_{WD} , which significantly increases during the outburst. In particular, the opening angle of the H II/H I boundary¹⁷ is proportional to \dot{M}_{WD}^{-2} (see Fig. 1 and Eq. (14) of Cariková & Skopal 2012).

In our case, the gradual decrease of \dot{M}_{WD} (see Fig. 6) suggests the gradual opening of bipolar, less dense ionized regions, already a few days after the outburst onset. This effect is indicated by a rapid decrease in the luminosity $L_{\text{WD}}^{\text{warm}}$ after t_{max} (see Table 3, Fig. 5 b). The flux of the warm WDP, $F_{\text{WD}}^{\text{warm}}(\lambda)$, was rapidly declining relative to the flux of the nebular continuum, $F_{\text{N}}(\lambda)$, especially in the blue part of the spectrum (see Figs. 3 and 4). For example, their ratio, $F_{\text{WD}}^{\text{warm}}/F_{\text{N}}$ at $\lambda = 4,700 \text{ \AA}$, decreased from ~ 30 on day 0.130 to ~ 0.7 on day 3.759 after t_{max} (see Fig. 9).

As the optically thin/thick interface between fast and slow (compressed) ejecta gradually opens, at some point, the angle of its opening will coincide with the line of sight (i.e., it will be equal to the orbital inclination, i). From this time on, we can see more into the central parts of the ejecta through the optically thinner medium, allowing us to directly observe the hot WDP. Such a situation probably occurred around day 4. This view is supported by the following results.

1. After this time, when the ionizing source (i.e., the hot WDP) rises above the optically thick horizon of the ejecta, the absorption in the direction towards the observer decreased significantly. This is supported by, (i) a rapid disappearance of the high-velocity absorption component of the hydrogen lines on day 3–4, which is created in the accumulated wind from the giant at the front of the expanding warm WDP by absorbing its light (see Fig. 13, Sect 4.6.2), (ii) a significant decrease in the flux absorbed by the narrow component from this time (see Fig. 7 e), and balancing the RV of the H β and H α line as the absorbing column rapidly decreased (see Sect. 3.5.2, Fig. 7 h), (iii) modeling of the X-ray NICER (0.5–10 keV) spectra showed a decrease in the hydrogen column density (N_{H}) on the line of sight by a factor of ~ 3.5 from \sim day 1

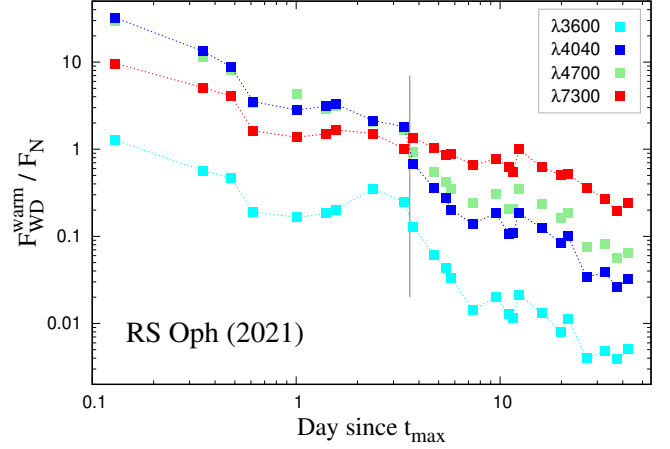


Figure 9. The ratio of fluxes from the warm WDP, $F_{\text{WD}}^{\text{warm}}$, and the nebula, F_{N} , at selected wavelengths, 3,600 Å, 4,040 Å, 4,700 Å, and 7,300 Å, given by SED models. The rapid decrease of this ratio indicates a rapid opening of bipolar ionized regions (see Sects. 4.3). The vertical line denotes a sudden change of this ratio between days 3.395 and 3.759, reflecting a change in the physical parameters of the warm WDP (see Sect. 4.6.2).

to \sim day 4–5 (see Fig. 6 of Orio et al. (2023) and Fig. 6 d of Islam et al. (2024)), and by (iv) a gradual increase in the hard X-ray flux measured by *Swift*-XRT and NICER to a maximum around day 5 (see Fig. 2 and 3 of Cheung et al. (2022) and Orio et al. (2023)), which also could be related to the gradual opening of the ionized shocked polar regions of the ejecta (see Sect. 4.6.2).

2. The first *IUE* spectrum, made on day 6.6, directly measured the stellar component of radiation from the hot WDP, which dominated the far-UV (see Fig. 4 d), confirming that the opening of the optically thin (\approx ionized) polar regions was larger than i within our interpretation.
3. Between day 3.395 and 3.759, the warm WDP cooled by $\sim 2,300 \text{ K}$, corresponding to an almost doubling of its effective radius (Table 3). Its emission shifted to the red part of the spectrum, while the nebular continuum began to dominate in the blue, leading to a flattening of the optical spectrum (see Figs. 3, 4, 9, 11, and 12). We interpret this significant temperature drop as a consequence of the rise of a cold, dense shell behind the internal shocks above the horizon of the compressed equatorial outflow, which thus began to contribute more to the thermal radiation from the weakening warm WDP (see Sect. 4.6.2).

¹⁷ We assume that the H II/H I boundary roughly corresponds to the optically thin/thick interface in the ejecta.

4.4. Density enhancement in the orbital plane

After the continuum flattened, the warm WDP was evident in the SED models as an extra component until the end of our observations (the solid blue line in Figs. 3 and 4). However, its luminosity and temperature gradually decreased, so that its presence was sometimes not necessary for SED modeling (day 31.349 and 33.361; Table 3, Fig. 4h). According to our interpretation of the ejecta evolution (Sect. 4.3), the continued expansion of the ejecta and the decrease in the mass-loss rate led to a dilution of the ejecta. Its optically densest part became geometrically thinner, forming a disk-like structure surrounding the WD in the equatorial (orbital) plane. According to our SED models, it can persist within the ejecta for a longer time until it becomes optically thin in the continuum and fully ionized (see Fig. 4) – the warm WDP disappears. However, a higher density in the equatorial region compared to the polar region persists. Moreover, the focusing of the stellar wind from the giant towards the orbital plane increases the density here, ahead of the ejecta¹⁸. This effect has been theoretically demonstrated in several studies (e.g., Booth et al. 2016, for RS Oph) as well as confirmed directly from observations (e.g., Shagatova et al. 2016). In our study, this effect is supported by narrow components in the spectral lines whose profile is not of the P-Cygni type (see Sects. 3.5.2 and 4.5).

The presence of the density enhancement on the orbital plane was directly indicated in 5 GHz radio imaging made by the European VLBI Network on day 34, when the wind from the giant, centered in the orbital plane, obscured the receding lobe of the bipolar ejecta (Munari et al. 2022). By analyzing the high-resolution imaging of the evolving bipolar outflows and assuming symmetry of both the approaching and receding lobes of the ejecta, Lico et al. (2024) estimated the density at/around the orbital plane as a function of radial distance from the binary, which is responsible for the flux attenuation between the lobes. After the 2006 explosion, by analyzing the Keck Interferometer Nuller observations on \sim day 3.8, Barry et al. (2008) also discussed the results in terms of a model that includes an increase in density in the orbital plane.

Finally, we note that the detection of increased density in the orbital plane from radio observations represents further independent indication of the focusing of the giant’s wind towards the orbital plane, which makes

the wind-mass-transfer in S-type symbiotic stars very efficient (see Skopal & Shagatova 2023, and references therein).

4.5. Surrounding wind environment

According to Munari (2025), the narrow emission component comes from the pre-existing RG wind, which may be ionized by the UV-flash photons generated approximately 1 day after the TNR onset, until the formation of expanding ejecta absorbs them (Kato et al. 2016)¹⁹. Accordingly, at this time (\sim time t_0), the maximum part of the giant wind is ionized. As a result, the first observations will always indicate a maximum flux of the narrow emission component. Its subsequent gradual decrease (Fig. 7e) is the result of ongoing recombinations in the ionized wind and the reduction in the volume of the undisturbed part of the wind due to the expansion of the ejecta. In the closest parts to the binary, up to distances of a few AU with densities of several times 10^{10} to 10^8 cm^{-3} (Booth et al. 2016), recombinations will occur on time scales of minutes to hours. In these parts, on the line of sight between the forming warm WDP and the observer, the value of N_{H} will therefore increase, which causes an increase in the absorption of light emitted by the underlying warm WDP – the flux absorbed by the narrow component increases. However, the expansion of the ejecta gradually shortens the column of undisturbed wind from the giant above the warm WDP, which slows down the growth of N_{H} . The resulting slight increase in absorption by the narrow component during the first days (see Fig. 7e) is therefore the result of the rivalry of these two processes – the neutralization of the initially ionized wind from time t_0 and the shortening of its column by the expansion of the ejecta. According to our interpretation of the evolution of the ejecta structure (Sect. 4.3), the value of N_{H} significantly reduces after around day 5, when the hot WDP starts ionizing the material on the line of sight. As a result, the flux absorbed in the undisturbed wind decreases significantly on a timescale of several days (Fig. 7e).

The evolution of the width of both narrow emission and absorption components follows the evolution of their fluxes. This is because the latter depends on the size of the column of emitting or absorbing material, as described above. Accordingly, in later stages of evolution, the column of undisturbed wind is further away from the binary, where theoretical models expect a smaller

¹⁸ Assuming the ejecta moves at a velocity of $\lesssim 1800 \text{ km s}^{-1}$ in the orbital plane (Chesneau et al. 2007), the front of the ejecta reaches a distance of $\lesssim 31 \text{ AU}$ on day 30.

¹⁹ We add that the hot WDP, which appears at early stages of the outburst and gives rise to strong nebular emission even before the optical maximum, can also ionize the surroundings of the binary (Sect. 3.2.2).

dispersion of RVs, and vice versa. Also, their very low fluxes correspond to smaller FWZI, since their wings are too weak to be measured accurately.

Finally, the RVs of the narrow emission lines (Fig. 7h) show interesting behavior. After subtracting the systemic velocity, the narrow emission is located between 24 and 35 km s⁻¹, around the terminal velocity of the RG wind. This means that the narrow emission component is emitted by the giant’s wind, which is mostly moving away from the observer, which is consistent with the non-P Cyg profile of narrow components (Sect. 3.5.2). The non-spherically symmetric distribution of the giant’s wind with a reduced density in the polar sides is also suggested by the hydrodynamic modeling of the wind-mass-transfer in symbiotic binaries (e.g., Booth et al. 2016; Bermúdez-Bustamante et al. 2020) and the finding from observations that the giant’s wind is focused towards the orbital plane at the expense of the polar regions (e.g., Shagatova et al. 2016; Munari et al. 2022).

4.6. Shocks in the RS Oph ejecta

4.6.1. A sketch of shocks in nova outflows

The detection of gamma rays in the early stages of nova evolution indicates the presence of shock waves inside the nova ejecta (e.g., Martin & Dubus 2013). According to recent studies (e.g., Metzger et al. 2014, 2015; Li et al. 2017; Martin et al. 2018; Chomiuk et al. 2021) aimed at explaining the nature of non-thermal emission (especially gamma rays) measured during the explosion of some CNe, we summarize the principle of shock waves formation in nova outflows as follows.

The shock model assumes the existence of an initial, relatively slow equatorially-focused outflow that is followed by a fast, more spherically symmetric outflow/wind. The fast wind then penetrates the previous, slower, and denser flow, generating an outwardly propagating forward-reverse shock structure, the so-called internal shocks. The shocks can accelerate a fraction of the charged particles to relativistic velocities that emit gamma rays through hadronic and leptonic interactions in a dense cold layer downstream of the shocks. The latter is the result of a rapid cooling of the hot shocked plasma by converting the rest of its energy into X-rays and UV emission. The cool gas collects behind the forward and reverse shocks, creating the so-called ‘cold central shell’. According to the shock dynamics, the cold central shell will quickly reach an approximate steady state with a constant velocity, identical to the velocity of shocks (see Eqs. (11) and (12) of Li et al. 2017). The harder thermal emission from the shocks is then absorbed and reprocessed by the dense slow ejecta ahead

of the shocks into optical emission (see Fig. 1 of Metzger et al. 2015).

The observed correlation between optical and γ -ray LCs around the optical maximum until several weeks after it (see Fig. 2 of Cheung et al. 2022) supports the above scenario and indicates that a significant fraction of the optical light comes from reprocessed shock emission. In the following section, we probe this property within our model.

4.6.2. Shocks in the wind-compression model of RS Oph

Figure 2 shows a sketch of the geometric and ionization structure of the RS Oph ejecta as inferred from our SED modeling (Sect. 3.2) and its interpretation (see Sects. 4.1 to 4.4). The location of the shocks and the cold central shell in the ejecta is outlined according to Fig. 1 of Metzger et al. (2015). The bipolar density and velocity distribution in the mass outflow, which is essential for the formation of shocks in the ejecta during nuclear outbursts on the WD surface, is fairly well demonstrated by observations (e.g., Schaefer et al. 2014; Chomiuk et al. 2014; Ribeiro et al. 2013, for CNe). Also, in less violent Z And-type outbursts in SySts, the ejected material expands more slowly in the equatorial region due to its compression here than material with reduced density in the polar regions. The former is indicated by the emergence of P Cyg profiles, while the latter is characterized by the broad emission wings of hydrogen lines during the outbursts; best documented for systems with high orbital inclination (see Skopal et al. 2006; Skopal 2006). However, the development of the bipolar structure from time t_0 has not been recorded yet.

Within our model, the process of wind compression into the orbital plane (i.e., the transition from spherical geometry at time t_0 to bipolar) occurs as fast as the wind expands. Already after 14 hours (day -0.366), the nebular emission was represented by bright hydrogen emissions, and on day 0.13 it was possible to estimate the amount of its continuum, which on day 0.617 clearly dominated the short-wave part of the spectrum (see Figs. 3d and 9 for $\lambda 3,600 \text{ \AA}$). The compressed equatorial part of the outflow/wind is cooled by recombinations and bremsstrahlung due to increasing density, and slowed down by increasing frictional forces. The continued fast wind emitted from the WD surface then penetrates the previously emitted, but already compressed and slowed wind, creating conditions for the formation of internal shocks.

Luminosity generated by shocks. According to the ejecta structure (Fig. 2) and the principle of shocks formation in it (Sect. 4.6.1), the luminosity of the warm WDP, $L_{\text{WD}}^{\text{warm}}$, in our model, should be comparable to

the luminosity of the internal shocks. Assuming that the velocity of the slow outflow is close to the velocity of the propagating shock, the total shock power, L_{sh} , is dominated by the reverse shock, i.e. (see Eq. (15) of Li et al. 2017),

$$L_{\text{sh}} = \frac{9}{32} f_{\Omega} \frac{f^{1/2} \dot{M}_{\text{WD}} (v_{\text{f}} - v_{\text{sh}})^3}{(1 - f_{\Omega}) v_{\text{f}}}, \quad (10)$$

where f_{Ω} is the fractional solid angle of the slow equatorially-focused outflow (i.e., $f = 1 - f_{\Omega}$ in Eq. (5)), $f^{1/2} \dot{M}_{\text{WD}} / (1 - f_{\Omega})$ is the spherical equivalent of the mass-loss rate, v_{f} is the velocity of the wind, and v_{sh} is the velocity of the propagating internal shock, assumed to be close to the expanding velocity of the cold central shell behind the shocks.

In our model, the optically thin polar part of the ejecta is gradually opening, which narrows the residual compressed part of the slow equatorial wind; the parameter f_{Ω} decreases. On \sim day 5 after t_0 , the opening angle of the optically thin/thick interface between the fast and slow (compressed) ejecta was approximately equal to $i = 52^\circ$ (see Sect. 4.3), which corresponds to $f_{\Omega} = 0.62$. In estimating L_{sh} , we adopted this value until day 4.7. Then, until day 13.4, we used $f_{\Omega} = 0.34$, and for the rest of the observations (day 16.9 to 43.5 after t_0) we chose $f_{\Omega} = 0.17$. Further, we used the values of \dot{M}_{WD} from Table 3, which correspond to $f = 1$, $v_{\text{f}} = 4,000 \text{ km s}^{-1}$ based on the terminal velocities of the broad H α wings (see Fig. 7 d), and for v_{sh} , according to Chesneau et al. (2007), we chose two limiting values, 0 and $1,800 \text{ km s}^{-1}$. Figure 10 shows a good agreement between the values of $L_{\text{WD}}^{\text{warm}}$ and L_{sh} for $v_{\text{sh}} = 1,800 \text{ km s}^{-1}$. However, it is likely that the actual values of L_{sh} are smaller than the values of $L_{\text{WD}}^{\text{warm}}$ determined directly from the spectrum, because the efficiency of generating shocks is expected to be higher near the equator due to the largest velocity difference, $v_{\text{f}} - v_{\text{sh}}$, than at higher latitudes of the slow outflow under the wind compression model.

The comparability of $L_{\text{WD}}^{\text{warm}}$ and L_{sh} values throughout the entire period, until the dispersion of the ejecta at the beginning of the SSS phase (Fig. 10), suggests that the slow equatorial outflow had been continuously replenished by the compression of the initially spherically-symmetric fast wind from the WD during this period. This result suggests that the wind compression model can create a bipolar structure of the outflow shortly after the ejection of the optically thick envelope at time t_0 , which can persist for a longer time. Its density and velocity contrasts, suitable for shock formation, are limited by the value of \dot{M}_{WD} . When the \dot{M}_{WD} drops significantly, the optically thick equatorial disk structure

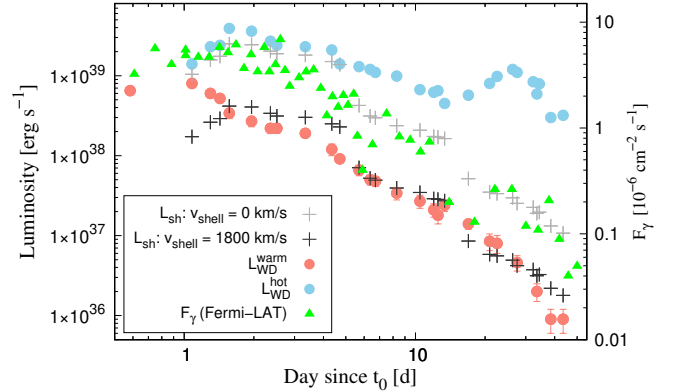


Figure 10. Comparison of the warm WDP luminosity ($L_{\text{WD}}^{\text{warm}}$, Table 3), the luminosity generated by internal shocks in the slow equatorial outflow (L_{sh} , Eq. (10)), and the Fermi-LAT γ -ray photon fluxes (F_{γ} , from Fig. 2 of Cheung et al. 2022) as a function of the nova age. The comparability of $L_{\text{WD}}^{\text{warm}}$ and L_{sh} , and their correlation with F_{γ} confirms that internal shocks generate a significant part of the luminosity of the warm WDP during its presence in the spectrum.

disappears²⁰, and shock formation and, hence, γ -rays are also significantly attenuated or disappear, creating conditions for observing SSS emission from the burning WD.

The cold central shell. The high cadence of our spectra allowed us to capture a sudden drop in the temperature of the warm WDP by $\sim 2,300 \text{ K}$ from day 3.395 to day 3.759 after t_{max} , but at a comparable luminosity and a much larger effective radius (see Table 3). The warm WDP emission shifted to longer wavelengths – the $F_{\text{WD}}^{\text{warm}}/F_{\text{N}}$ ratio suddenly decreased in the blue part of the spectrum ($\lambda 3,600 - 4,700 \text{ \AA}$), but increased at $\lambda 7,300 \text{ \AA}$ (see Fig. 9). Within the internal shocks model in the compressed wind (Fig. 2), this effect could be interpreted as a result of narrowing the slower dense outflow to the equator, below the line of sight (i.e., $f_{\Omega} < 0.62$), when the radiation from the warm WDP weakens as it is viewed from the side. In contrast, radiation from the cold, dense shell behind the internal shocks becomes visible when viewing the slow outflow from above at later times ($>$ day 4–5 after t_0) and can thus contribute to the warm thermal radiation. This explanation is supported by the long-lasting presence of the very cold radiation in the spectrum ($T_{\text{BB}} \sim 5,200 - 3,600 \text{ K}$; the blue line in Figs. 3 and 4), whose contribution de-

²⁰ In the same way, the enhanced value of \dot{M}_{WD} during Z And-type outbursts in SySts is responsible for the formation of an optically thick disk-like structure in the orbital plane, which disappears as the \dot{M}_{WD} decreases, and the system enters a quiescent phase (see Sect. 3.1 of Cariková & Skopal 2012).

creases along with the Fermi-LAT γ -ray radiation. Also, the *Swift*-XRT emission (2–10 keV) from the hot base of the internal reverse shock should be better observed at $f_\Omega < 0.62$ because it suffers from less absorption, which would explain the shift of its maximum to days 5–6 after t_0 (see Fig. 2 of Cheung et al. 2022).

External shocks. In the case of symbiotic binaries, the ejecta penetrates the surrounding relatively stable and thin stellar wind from the giant, generating external shocks at the expense of its kinetic energy. The high-velocity absorptions observed in the H α profile during the first 3–4 days (see Fig. 13) probably originate in the cold absorbing shell accumulated behind the external shocks (Sect. 3.5.1), which represents their manifestation in the optical spectrum at a very early stage. The evolution of the broad H α component indicates a relatively small deceleration of the ejecta in the line of sight due to external shocks – the broad wings are still present, although very weak (see Fig. 8), with only a slight decrease of its terminal velocity to about 4,000 km s $^{-1}$ (Fig. 7 d). The small deceleration of the ejecta indicated by the H α line profile is likely a consequence of the significant dilution of the wind from the giant in the polar regions.

5. SUMMARY

In this work, we focused on the analysis of the optical continuum of the recurrent symbiotic nova RS Oph during its recent 2021 explosion, from 9 hours before the brightness maximum to the SSS phase (\sim day 42). Using the method of the multi-wavelength SED modeling, we determined the ionization structure of the ejecta and its physical parameters as a function of the nova age (Figs. 2, 3, 4, 5, 6, Table 3). Additional properties of the ejecta and the surrounding environment were obtained by analyzing the evolution of the H α line using medium to very high resolution spectroscopy (Sects. 3.5, and 4.5). The main results of our analysis can be summarized as follows.

1. On day -0.366 (i.e., 9 hours before t_{\max} or 14 hours after t_0), the warm WD pseudophotosphere (warm WDP, see Sect. 3.2) resembled an A-type star with T_{eff} of $\sim 11,000$ K, inflated to $\sim 114 (d/1.6 \text{ kpc}) R_\odot$, generating luminosity of $L_{\text{WD}}^{\text{warm}} \sim 7 \times 10^{38} (d/1.6 \text{ kpc})^2 \text{ erg s}^{-1}$. On day $+0.130$ (3 hours after t_{\max}), the T_{eff} of the warm WDP dropped to $\sim 7,250$ K and its effective radius $R_{\text{WD}}^{\text{eff}}$ (see Sect 3.2.1) reached a maximum of $\sim 290 (d/1.6 \text{ kpc}) R_\odot$. The estimate of the nebular continuum emission measure, $EM \gtrsim 10^{62} (d/1.6 \text{ kpc})^2 \text{ cm}^{-3}$, limited the luminosity of the hot WD pseudophotosphere

$L_{\text{WD}}^{\text{hot}}$ (hot WDP, see Sect. 3.2) to $\gtrsim 1.4 \times 10^{39} (d/1.6 \text{ kpc})^2 \text{ erg s}^{-1}$, and the mass-loss rate \dot{M}_{WD} to $\gtrsim 2.3 \times 10^{-4} M_\odot \text{ yr}^{-1}$. During the next 12 hours (day 0.617), EM and $L_{\text{WD}}^{\text{hot}}$ increased by a factor of >3 , reached their maximum, and the nebular continuum began to rival the radiation from the warm WDP (see Fig. 4 a). The corresponding maximum value of \dot{M}_{WD} was $\sim 5 \times 10^{-4} M_\odot \text{ yr}^{-1}$. Integrating \dot{M}_{WD} from day 0.13 to day 42.6 corresponds to an average value of the ejected ionized mass of $1.2 \times 10^{-5} M_\odot$ (Sects. 3.3, 3.4, and Fig. 6).

2. Disentangling the spectrum into the stellar and nebular components of radiation from the very beginning of the explosion revealed the biconical structure of the ejecta: A flared density-enhanced disk-like structure around the equator, whose outer rim (i.e., the warm WDP) obscures a strong ionizing source (i.e., the hot WDP) in the line of sight, whose radiation ionizes the rarefied polar regions giving rise to the strong nebular emission (Sect. 4.1, Fig. 2). We explain the bipolar structure of the ejecta and its evolution by rotation of the accreting WD, which leads to a compression of the outflowing wind towards the equatorial plane (see Sects. 4.2, and 4.3).
3. On \sim day 4 (or \sim day 5 after t_0), the continuum suddenly flattened (Fig. 11), the T_{BB} of the warm WDP dropped by $\sim 2,300$ K with subsequent gradual decline of its luminosity and cooling (Table 3, Figs. 4 and 5 d). Simultaneously, a significant decrease in absorption towards the observer was indicated, and the hot WDP became directly observable. According to the ejecta evolution (see Sect. 4.3), these effects can be caused by narrowing the optically thick equatorial outflow below the line of sight (i.e., the fractional solid angle $f_\Omega < 0.62$, see Eq. (10)). Accordingly, the sudden change in T_{BB} can be interpreted by the direct visibility of the cold dense shell behind the internal shocks (see Fig. 2) after \sim day 4. The comparability of $L_{\text{WD}}^{\text{warm}}$ with the luminosity of the internal shocks L_{sh} (Eq. (10)) and their correlation with the Fermi-LAT γ -ray fluxes until \sim day 42, support this interpretation (see Fig. 10, Sect. 4.6.2).
4. Very high resolution UVES spectra ($R \gtrsim 10^5$) showed that the profile of the narrow line components is not of the P Cyg type (see Fig. 8). This fact, and the position of the narrow emission component near the terminal velocity of the RG wind are consistent with the non-spherically symmetric distribution of the giant’s wind with a reduced

density in the polar regions (see Sects. 3.5.2, 4.4, and 4.5).

The wind compression model (Sect. 4.2, Fig. 2) represents a promising mechanism shaping the bipolar structure of the ejecta from very early stages, with sufficient density and velocity contrasts to generate internal shocks. Our UV/optical/near-IR continuum analysis (Sect. 3.2) confirmed the presence of strong internal shocks that form within the compressed, slower equatorial outflow, the power of which is comparable with the warm WDP luminosity from the maximum until our last observations on day 42 (see Sect. 4.6.2, and Fig. 10). We conclude that the disentangling method allows us to specify the efficiency and evolution of γ -ray emission more precisely, and to estimate the structure of mass ejection in novae.

ACKNOWLEDGMENTS

The authors thank the anonymous referee for useful comments. This work was supported by a grant of the Slovak Academy of Sciences, VEGA No. 2/0003/25, and by the Slovak Research and Development Agency under the contracts No. APVV-20-0148, and APVV-24-0160. The research of MW was partially supported by the project Cooperatio – Physics of Charles University in Prague. The amateur spectra presented in this paper were obtained within the *Astronomical Ring for Access to Spectroscopy (ARAS)*, an initiative promoting cooperation between professional and am-

ateur astronomers in the field of spectroscopy. The authors thank ARAS observers for their contributions made within the ARAS program coordinated by Francois Teyssier. This paper is in part based on data from Paranal Observatory, ESO, Chile. The observations have been taken under a target opportunity program 105.20B6.001, 105.20B6.002, PI Paolo Molaro. We obtained the spectra from the ESO Science Archive Facility with DOI: <https://doi.org/10.18727/archive/50>. This publication also uses ultraviolet spectroscopy made with the *International Ultraviolet Explorer*, obtained from the MAST data archive at the Space Telescope Science Institute, which is operated by the Association of Universities for Research in Astronomy, Inc., under NASA contract NAS5-26555. We also acknowledge the variable-star observations from the AAVSO International Database contributed by observers worldwide and used in this research.

AUTHOR CONTRIBUTIONS

AS was responsible for data analysis and interpretation, and for writing the initial draft of the manuscript. MV, FT, MF, MŠ, and MW contributed to the acquisition and processing of spectroscopic observations (see Sect. 2.2). SS contributed to the acquisition and processing of the photometric observations (see Sect. 2.1, and Appendix A).

Facilities: IUE, AAVSO, ARAS, Perek:2m, UT2 Kueyen:8m

APPENDIX

A. MULTICOLOR OPTICAL PHOTOMETRY

In this appendix, we present the table with our multicolor $UBVR_CI_C$ photometry of RS Oph during its 2021 outburst (see Sect. 2.1, Table 4).

B. SPECTRA CALIBRATION

To calibrate the spectra in relative units (mostly the low-resolution spectra in Table 6), it is necessary to know the absolute flux at least at one wavelength. For this purpose, we used multicolor photometry acquired simultaneously with the spectrum. Due to the presence of emission lines in the spectrum, we first eliminated their influence on the true continuum. According to the method of Skopal (2007), we determined corrections for emission lines, $\Delta m = m_{\text{obs}} - m_{\text{cont}}$, where m_{obs} is the observed magnitude, and m_{cont} is the magnitude of the true continuum. Their values are listed in Table 5. Then we converted the emission-line-free UBV and R_CI_C magnitudes to fluxes according to the calibration of Henden & Kaitchuck (1982) and Bessell (1979), respectively. In most cases, we scaled the spectra to the dereddened and emission-line-free fluxes obtained from the V magnitudes. Fluxes from other photometric filters served as a verification of the continuum profile. A systematic flux shift in the B filter (up to 10–15% above the continuum) was probably caused by the blending of emission lines in this region.

Having the low-resolution spectra calibrated, we determined absolute fluxes in the continuum at the wavelengths of selected emission lines along the outburst (see Fig 11). Using these calibration curves, we can calibrate the cor-

Table 4. $UBVR_C I_C$ photometry of RS Oph obtained at the Stará Lesná Observatory during its 2021 outburst.

HJD	Date	U		B		V		R_C		I_C	
2 459...	mm-dd.ddd	mag	error	mag	error	mag	error	mag	error	mag	error
464.296	09-06.796	9.284	0.070	9.644	0.063	9.164	0.058	7.350	0.088	7.458	0.073
467.256	09-09.756	9.564	0.056	9.926	0.048	9.379	0.043	7.588	0.079	7.667	0.063
476.265	09-18.765	9.989	0.053	10.310	0.045	9.743	0.039	8.020	0.075	8.057	0.060
490.225	10-02.725	10.442	0.049	10.664	0.044	10.090	0.037	8.484	0.069	8.388	0.059
493.218	10-05.718	10.499	0.043	10.693	0.037	10.073	0.028	8.534	0.064	8.393	0.055
496.216	10-08.716	10.551	0.036	10.786	0.029	10.124	0.019				
500.206	10-12.706	10.696	0.034	10.870	0.029	10.201	0.018	8.692	0.058	8.527	0.050
503.209	10-15.709	10.753	0.036	10.968	0.029	10.259	0.017	8.795	0.056	8.591	0.048
512.193	10-24.693	10.939	0.042	11.106	0.038	10.485	0.028	9.051	0.059	8.784	0.054
514.191	10-26.691	11.063	0.039	11.201	0.035	10.531	0.022	9.079	0.056	8.812	0.051
517.182	10-29.682	11.154	0.038	11.351	0.033	10.685	0.021	9.237	0.057	8.950	0.052
519.179	10-31.679	11.238	0.043	11.396	0.039	10.772	0.029	9.331	0.061	9.057	0.056
524.181	11-05.681	11.633	0.046	11.711	0.041	11.001	0.023	9.637	0.058	9.291	0.056

responding regions in the medium-resolution spectra by interpolating adjacent continuum fluxes to the time of their acquisition.

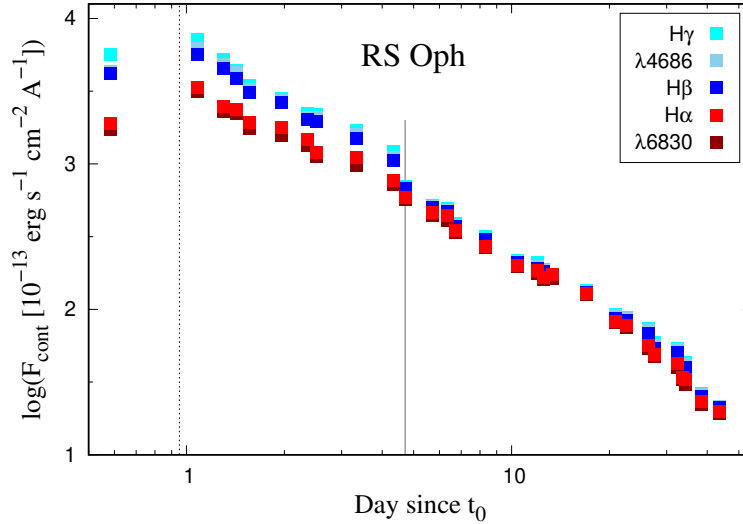


Figure 11. Evolution of the continuum fluxes, $F_{\text{cont.}}$, at/around selected emission lines (see keys) given by SED models. The vertical dotted line indicates the time of the optical maximum (see Table 2), and the gray line at day 4.7 denotes the time of spectrum flattening, when the continuum fluxes in the blue part (at $H\gamma$ and $H\beta$) became nearly equal to those in the red part (at $H\alpha$ and $\lambda 6,830$).

C. EVOLUTION OF THE OPTICAL CONTINUUM ON THE UVES SPECTRA

In this appendix, we present a figure showing the evolution of the RS Oph continuum from just after t_{max} (day 0.617) to our last observation (day 42.566). In this example, we used high-resolution UVES spectra smoothed with a 1 Å filter which show the range from 3,200 to 9,500 Å (see Figure 12). Our SED models in the figure are given by the parameters in Table 3, determined by Eq. (1) or (2).

Table 5. Corrections of the U , B , V , and R_C magnitudes for emission lines measured on the spectra in Tables 6 and 7.

Age ^a (days)	Sp. range (nm)	ΔU (mag)	ΔB (mag)	ΔV (mag)	ΔR_C (mag)
-0.366	390 - 724	–	–	-0.012	-0.005
0.130	370 - 860	–	-0.016	-0.002	-0.026
0.348	390 - 750	–	-0.077	-0.016	-0.031
0.478	371 - 739	–	-0.082	-0.023	-0.042
0.617	304 - 946	-0.005	-0.120	-0.084	-0.069
1.006	366 - 880	-0.005	-0.110	-0.057	-0.103
1.409	364 - 785	-0.006	-0.332	-0.107	-0.154
1.567	304 - 946	-0.019	-0.220	-0.096	-0.195
2.391	330 - 855	-0.029	-0.247	-0.118	-0.292
3.395	330 - 855	-0.049	-0.272	-0.116	-0.439
3.759	304 - 946	-0.040	-0.371	-0.142	-0.495
4.751	304 - 946	-0.065	-0.405	-0.211	-0.590
5.416	330 - 855	-0.064	-0.452	-0.186	-0.545
5.759	304 - 946	-0.074	-0.529	-0.300	-0.673
7.343	385 - 750	–	-0.489	-0.277	-0.746
9.510	304 - 946	-0.085	-0.614	-0.397	-0.915
11.048	360 - 875	-0.039	-0.487	-0.320	-0.866
11.559	304 - 946	-0.110	-0.585	-0.332	-0.904
12.421	330 - 855	-0.077	-0.559	-0.331	-0.877
15.998	355 - 874	-0.068	-0.610	-0.355	-0.661
19.989	357 - 880	-0.088	-0.758	-0.429	-0.720
21.583	304 - 946	-0.189	-0.772	-0.346	-0.596
25.356	330 - 855	-0.142	-0.854	-0.426	-1.144
26.559	304 - 946	-0.217	-0.849	-0.444	-1.171
31.349	330 - 855	-0.261	-0.669	-0.428	-1.145
32.549	304 - 946	-0.267	-0.907	-0.473	-1.225
33.361	370 - 750	–	-0.650	-0.394	-1.072
37.532	304 - 946	-0.284	-0.889	-0.528	-1.225
42.566	304 - 946	-0.320	-0.930	-0.566	-1.350

Notes. ^a As in Table 3.

D. EVOLUTION OF THE $H\alpha$ AND $H\beta$ LINE PROFILES

In this appendix, we present a figure showing the evolution of the $H\alpha$ and $H\beta$ line profiles during the first hours and days of the RS Oph explosion in 2021 (see Figure 13).

E. TABLES OF SPECTROSCOPIC OBSERVATIONS

In this appendix, we present tables of spectroscopic observations used in this study (see Tables 6, 7, and 8).

F. PARAMETERS OF THE $H\alpha$ LINE

In this appendix, we present a table of $H\alpha$ line parameters (see Table 9).

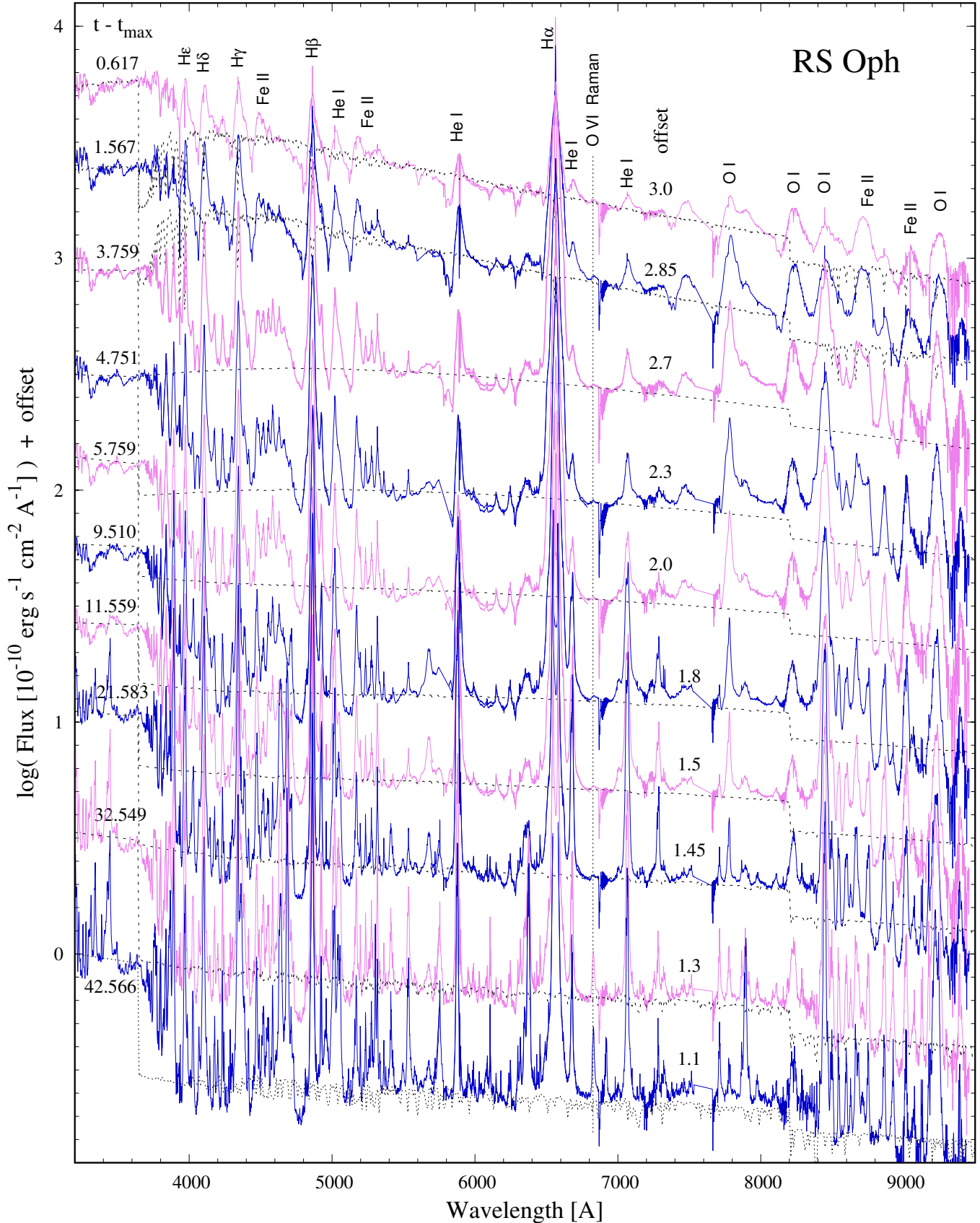


Figure 12. The evolution of the RS Oph optical spectrum measured by the UVES spectrograph from day 0.617 to day 42.566. A strong nebular continuum is indicated by the Balmer jump in emission. It dominates the spectrum from day 3.7, when the overall continuum flattens (see also Fig. 11). Dotted lines represent our SED models (Eq. (1) or (2) for parameters in Table 3).

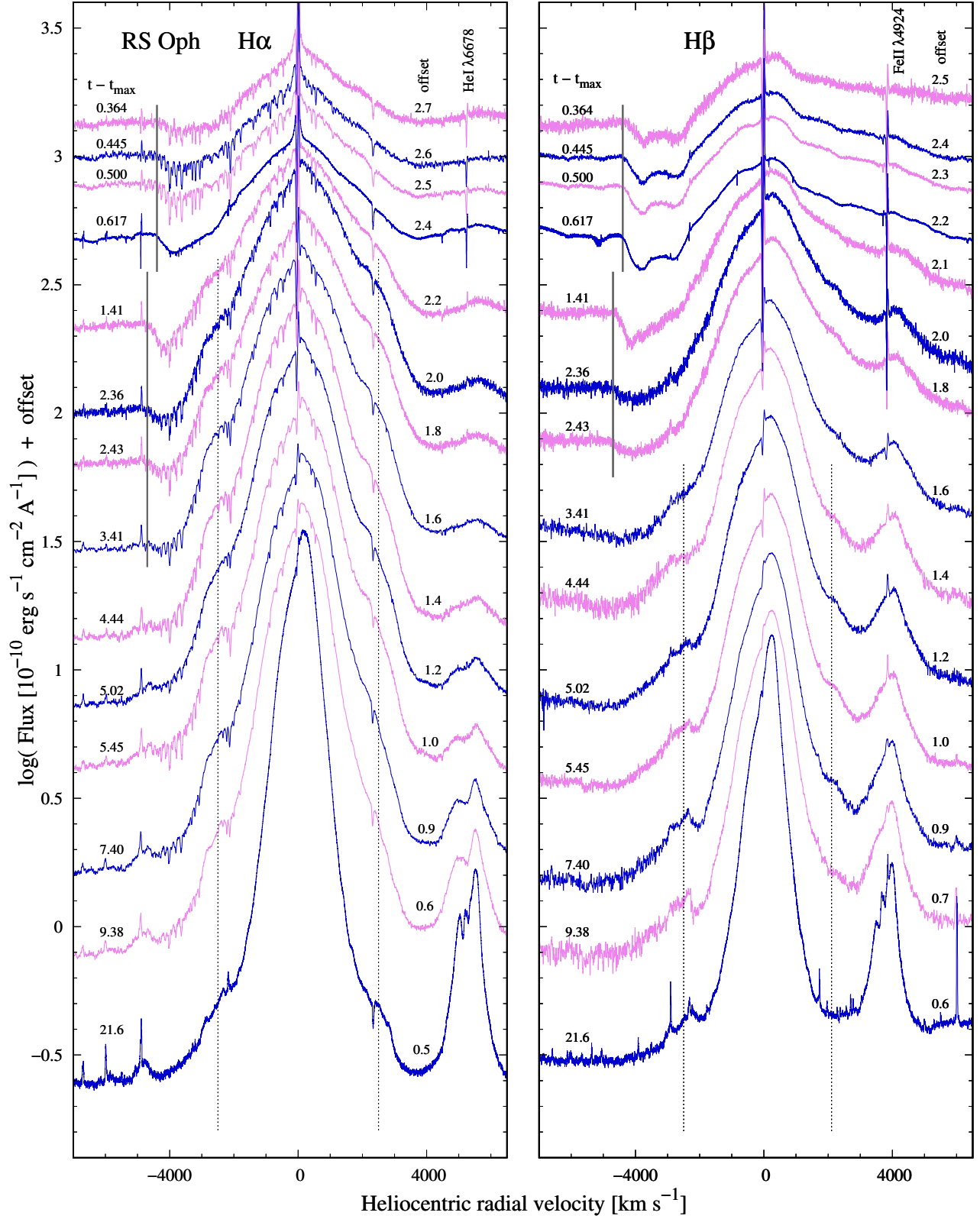


Figure 13. Evolution of the H α (left) and H β (right) line profiles during the first hours and days of the RS Oph explosion. Vertical gray lines denote the terminal velocity of the broad absorption component, while the dotted lines denote emission bumps located around $\pm 2,500 \text{ km s}^{-1}$.

Table 6. Log of low-resolution spectroscopic observations[†]

Age ^a JD-JD _{max}	JD 2,459...	Date ^b mm-dd.ddd	Range [nm]	Obs. ^c
-0.366	435.594	08-09.094	390 - 724	(i)
0.130	436.090	08-09.590	370 - 860	(ii)
0.348	436.308	08-09.808	390 - 750	(iii)
0.478	436.438	08-09.938	371 - 739	(iv)
1.006	436.966	08-10.466	366 - 880	(ii)
1.361	437.321	08-10.821	390 - 750	(iii)
1.431	437.392	08-10.891	364 - 500	(v)
1.435	437.395	08-10.895	375 - 785	(vi)
2.375	438.335	08-11.835	330 - 570	(vii)
2.406	438.366	08-11.866	570 - 855	(vii)
3.388	439.348	08-12.848	330 - 570	(vii)
3.401	439.361	08-12.861	570 - 855	(vii)
5.404	441.364	08-14.864	330 - 570	(vii)
5.428	441.388	08-14.888	570 - 855	(vii)
7.343	443.303	08-16.803	385 - 750	(iii)
11.048	447.008	08-20.508	360 - 875	(ii)
12.414	448.374	08-21.874	330 - 570	(vii)
12.427	448.387	08-21.887	570 - 855	(vii)
15.998	451.958	08-25.458	355 - 874	(ii)
19.989	455.949	08-29.449	357 - 880	(ii)
25.343	461.303	09-03.803	330 - 570	(vii)
25.368	461.328	09-03.828	570 - 855	(vii)
31.333	467.293	09-09.793	330 - 570	(vii)
31.365	467.325	09-09.825	570 - 855	(vii)
33.361	469.321	09-11.821	370 - 750	(viii)

Notes.

[†] Resolving power from 500 to 1300 (Table 1), ^(a) as in Table 3, ^(b) month and day of 2021 – the mid of exposure in UT, ^(c) label of the observatory (Table 1).

Table 7. Log of high-resolution UVES spectra[†]

Age ^a JD-JD _{max}	JD 2,459...	Date ^b mm-dd.ddd	Grism ^c	T_{exp} (s)
0.614	436.574	08-10.074	CD1	60
0.614	436.574	08-10.074	CD3	40
0.619	436.579	08-10.079	CD2	15
0.619	436.579	08-10.079	CD4	15
1.561	437.521	08-11.021	CD1	30
1.561	437.521	08-11.021	CD3	10
1.565	437.525	08-11.025	CD2	10
1.565	437.525	08-11.025	CD4	4
1.574	437.534	08-11.034	CD4	2
3.755	439.715	08-13.215	CD3	180
3.755	439.715	08-13.215	CD1	360
3.762	439.722	08-13.222	CD4	60
3.762	439.722	08-13.222	CD2	60
4.748	440.708	08-14.208	CD3	180
4.748	440.708	08-14.208	CD1	360
4.755	440.715	08-14.215	CD4	60
4.755	440.715	08-14.215	CD2	60
5.755	441.715	08-15.215	CD3	360
5.755	441.715	08-15.215	CD1	480
5.763	441.723	08-15.223	CD4	120
5.763	441.723	08-15.223	CD2	120
9.506	445.466	08-18.966	CD3	360
9.506	445.466	08-18.966	CD1	480
9.513	445.473	08-18.973	CD4	120
9.513	445.473	08-18.973	CD2	120
11.551	447.511	08-21.011	CD3	360
11.551	447.511	08-21.011	CD1	480
11.567	447.527	08-21.027	CD4	120
11.567	447.527	08-21.027	CD2	120
21.579	457.539	08-31.039	CD1	480
21.587	447.547	08-31.047	CD2	120
21.578	447.538	08-31.038	CD3	360
21.587	457.547	08-31.047	CD4	120
26.554	462.514	09-05.014	CD1	480
26.564	462.524	09-05.024	CD2	120
26.554	462.514	09-05.014	CD3	360
26.563	462.523	09-05.023	CD4	120
32.530	468.490	09-10.990	CD1	600
32.556	468.516	09-11.016	CD2	180
32.543	468.503	09-11.003	CD3	240
32.559	468.519	09-11.019	CD4	15
32.556	468.516	09-11.016	CD4	180
37.535	473.495	09-15.995	CD1	600
37.529	473.489	09-15.989	CD2	180
37.535	473.495	09-15.995	CD3	540
37.532	473.492	09-15.992	CD4	5
37.529	473.489	09-15.989	CD4	180
42.558	478.518	09-21.018	CD1	600
42.570	478.530	09-21.030	CD2	180
42.558	478.518	09-21.018	CD3	540
42.573	478.533	09-21.033	CD4	5
42.570	478.530	09-21.030	CD4	180

Notes. [†] Resolving power from 58,640 to 107,200, ^(a) as in Table 1, ^(b) month and day of 2021 – the start of exposure in UT, ^(c) corresponding spectral ranges are 304–392, 373–500, 473–684 and 566–946 nm for grism CD1, CD2, CD3 and CD4.

Table 8. Log of medium-resolution spectroscopic observations[†]

Age ^a	JD	Date ^b	Range	Obs. ^c
JD-JD _{max}	2,459...	mm-dd.ddd	[nm]	
0.364	436.324	08-09.824	420-736	(ix)
0.378	436.338	08-09.838	420-736	(ix)
0.389	436.349	08-09.849	641-688	(Ondrejov)
0.392	436.352	08-09.852	420-736	(ix)
0.406	436.366	08-09.866	420-736	(ix)
0.412	436.372	08-09.872	374-975	(x)
0.420	436.380	08-09.880	420-746	(ix)
0.422	436.382	08-09.882	392-760	(xi)
0.422	436.382	08-09.882	641-688	(Ondrejov)
0.434	436.394	08-09.894	420-736	(ix)
0.444	436.404	08-09.904	400-761	(xii)
0.445	436.405	08-09.905	392-760	(xi)
0.472	436.432	08-09.932	400-761	(xii)
0.481	436.441	08-09.941	394-894	(xiii)
0.494	436.454	08-09.954	400-761	(xii)
0.500	436.460	08-09.960	392-760	(xi)
0.513	436.473	08-09.973	394-894	(xiii)
0.546	436.506	08-10.006	394-894	(xiii)
1.364	437.324	08-10.824	420-736	(ix)
1.378	437.338	08-10.838	420-746	(ix)
1.390	437.350	08-10.850	392-752	(xii)
1.392	437.352	08-10.852	420-736	(ix)
1.406	437.366	08-10.866	420-736	(ix)
1.420	437.380	08-10.880	420-746	(ix)
1.434	437.394	08-10.894	420-736	(ix)
1.460	437.420	08-10.920	392-752	(xii)
2.059	438.019	08-11.519	650-674	(xiv)
2.360	438.320	08-11.820	420-746	(ix)
2.375	438.335	08-11.835	420-746	(ix)
2.389	438.349	08-11.849	420-746	(ix)
2.403	438.363	08-11.863	420-746	(ix)
2.409	438.369	08-11.869	430-752	(xii)
2.418	438.378	08-11.878	420-746	(ix)
2.432	438.392	08-11.892	420-736	(ix)
2.485	438.445	08-11.945	648-664	(xv)
3.386	439.346	08-12.846	641-688	(Ondrejov)
3.414	439.374	08-12.874	387-894	(xiii)
3.449	439.409	08-12.909	647-698	(xvi)
3.455	439.415	08-12.915	648-664	(xv)
3.488	439.448	08-12.948	392-760	(xi)
4.363	440.323	08-13.823	420-736	(ix)
4.369	440.329	08-13.829	626-674	(Ondrejov)
4.392	440.352	08-13.852	420-736	(ix)
4.406	440.366	08-13.866	420-736	(ix)
4.420	440.380	08-13.880	420-746	(ix)
4.424	440.384	08-13.884	398-758	(xi)
4.434	440.394	08-13.894	420-746	(ix)
4.439	440.399	08-13.899	400-890	(xiii)
4.493	440.453	08-13.912	640-667	(vii)
5.018	440.978	08-14.478	400-741	(xvii)
5.343	441.303	08-14.803	626-674	(Ondrejov)
5.378	441.338	08-14.838	400-761	(xii)
5.409	441.369	08-14.869	619-688	(xviii)
5.423	441.383	08-14.883	420-736	(ix)
5.425	441.385	08-14.885	400-761	(xii)
5.452	441.412	08-14.912	392-759	(xi)
6.444	442.404	08-15.904	378-948	(x)
7.368	443.328	08-16.828	648-664	(xvi)

Table 8. continued

Age ^a JD-JD _{max}	JD 2 459...	Date ^b mm-dd.ddd	Range [nm]	Obs. ^c
7.371	443.331	08-16.831	430-735	(ix)
7.397	443.357	08-16.857	394-894	(xiii)
8.388	444.348	08-17.848	395-890	(xiii)
8.402	444.362	08-17.862	643-677	(xvi)
9.384	445.344	08-18.844	387-894	(xiii)
9.724	445.684	08-19.184	648-664	(xix)
10.400	446.360	08-19.860	420-890	(xiii)
10.473	446.433	08-19.933	648-664	(xv)
11.395	447.355	08-20.855	473-735	(ix)
11.431	447.391	08-20.891	387-894	(xiii)
11.440	447.400	08-20.900	648-669	(xv)
11.711	447.671	08-21.171	648-664	(xix)
12.355	448.315	08-21.815	641-688	(Ondrejov)
12.366	448.326	08-21.826	641-688	(Ondrejov)
12.456	448.416	08-21.916	387-894	(xiii)
13.147	449.107	08-22.607	400-740	(xvii)
13.467	449.427	08-22.927	387-894	(xiii)
14.402	450.362	08-23.862	420-890	(xiii)
15.419	451.379	08-24.879	392-759	(xi)
15.456	451.416	08-24.916	648-663	(xv)
16.374	452.334	08-25.834	475-735	(ix)
16.439	452.399	08-25.899	392-759	(xi)
16.448	452.408	08-25.908	648-663	(xv)
17.384	453.344	08-26.844	387-894	(xiii)
18.431	454.391	08-27.891	648-663	(xv)
18.452	454.412	08-27.912	392-759	(xi)
19.356	455.316	08-28.816	475-735	(ix)
19.376	455.336	08-28.836	381-894	(xiii)
20.373	456.333	08-29.833	381-894	(xiii)
22.085	458.045	08-31.545	650-674	(xiv)
22.420	458.380	08-31.880	648-663	(xv)
23.347	459.307	09-01.807	475-735	(ix)
23.381	459.341	09-01.841	392-759	(xi)
24.317	460.277	09-02.777	641-688	(Ondrejov)
24.386	460.346	09-02.846	392-759	(xi)
24.422	460.382	09-02.882	648-663	(xv)
25.417	461.377	09-03.877	381-894	(xiii)
26.378	462.338	09-04.838	381-894	(xiii)
27.375	463.335	09-05.835	392-892	(xiii)
27.407	463.367	09-05.867	392-759	(xi)
28.394	464.354	09-06.854	392-759	(xi)
29.345	465.305	09-07.805	644-666	(xx)
30.391	466.351	09-08.851	387-893	(xiii)
31.336	467.296	09-09.796	641-688	(Ondrejov)
31.397	467.357	09-09.857	644-666	(xx)
32.389	468.349	09-10.849	381-886	(xiii)
34.379	470.339	09-12.839	402-894	(xiii)
35.331	471.291	09-13.791	644-666	(xx)
35.995	471.955	09-14.455	400-741	(xvii)
38.328	474.288	09-16.788	644-666	(xx)
38.335	474.295	09-16.795	648-664	(xxi)
41.071	477.031	09-19.531	400-741	(xvii)
41.390	477.350	09-19.850	410-890	(xiii)
44.040	480.000	09-22.500	400-741	(xvii)
47.311	483.271	09-25.771	641-688	(Ondrejov)

Notes. † Resolving power from 8,500 to 20,000 (Table 1), ^(a) as in Table 3, ^(b) as in Table 6, ^(c) label of the observatory (Table 1, Sect. 2.2).

Table 9. Parameters of the H α line profile

Age ^a	Date ^b	F_{α}^c	$F_{\text{cont.}}^d$	FWHM ^e	v_{∞}^f	RV_{abs}^g	RV_{em}^g	F_{abs}^h	F_{em}^h	\dot{M}_{WD}^i	Obs. ^j
0.364	0809.824	15.74	2.598	55.40	-4,448	-74.95	-11.91	0.94	12.27	1.57	(ix)
0.378	0809.838	16.66	2.570	57.20	-4,424	-75.44	-11.94	0.88	12.89	1.62	(ix)
0.389	0809.849	15.79	2.548	55.64	-4,738	-73.96	-11.37	0.71	11.95	1.69	(Ondrejov)
0.392	0809.852	15.98	2.542	57.35	-4,351	-75.01	-12.43	0.88	12.25	1.56	(ix)
0.406	0809.866	15.47	2.514	57.20	-4,430	-76.42	-13.38	0.91	12.52	1.57	(ix)
0.412	0809.872	16.16	2.502	57.05	-4,595	-75.97	-13.39	0.84	12.41	1.66	(x)
0.420	0809.880	15.52	2.486	57.70	-4,358	-75.08	-12.96	0.82	12.17	1.55	(ix)
0.422	0809.882	15.49	2.482	58.60	-4,221	-80.11	-13.87	0.66	12.24	1.50	(xi)
0.422	0809.882	15.68	2.482	59.10	-4,736	-74.41	-12.29	0.90	12.39	1.55	(Ondrejov)
0.434	0809.894	15.63	2.458	57.55	-4,219	-76.02	-13.44	0.93	12.39	1.51	(ix)
0.444	0809.904	16.92	2.438	60.00	-4,370	-74.67	-11.18	1.10	12.06	1.63	(xii)
0.445	0809.905	15.27	2.436	59.10	-4,398	-78.34	-13.47	0.93	11.58	1.55	(xi)
0.472	0809.932	17.48	2.382	58.55	-4,395	-74.29	-12.16	1.18	11.37	1.67	(xii)
0.481	0809.941	18.50	2.367	59.70	-4,444	-73.50	-9.55	1.12	12.09	1.74	(xiii)
0.494	0809.954	18.45	2.352	59.45	-4,383	-75.24	-12.66	1.23	11.70	1.74	(xii)
0.500	0809.960	17.44	2.345	59.95	-4,397	-76.62	-12.21	0.83	11.57	1.70	(xi)
0.513	0809.973	19.74	2.330	59.78	-4,434	-72.59	-9.10	1.14	12.67	1.85	(xiii)
0.546	0810.006	20.94	2.293	59.65	-4,484	-72.94	-9.87	1.05	11.23	1.98	(xiii)
0.617	0810.076	18.83	1.919	59.63	-4,497	-74.24	-12.57	2.02	10.97	1.99	(Paranal)
1.364	0810.824	34.45	1.470	58.28	-4,592	-72.52	-11.08	1.89	8.37	2.52	(ix)
1.378	0810.838	34.77	1.470	58.10	-4,619	-72.09	-11.79	1.94	8.00	2.53	(ix)
1.390	0810.850	34.10	1.470	56.10	-4,657	-72.12	-11.37	2.86	8.35	2.52	(xii)
1.392	0810.852	35.10	1.470	58.40	-4,630	-73.04	-12.28	1.99	8.01	2.55	(ix)
1.406	0810.866	34.72	1.470	58.25	-4,665	-73.31	-11.41	2.04	7.82	2.54	(ix)
1.420	0810.880	35.18	1.470	58.30	-4,618	-73.56	-12.35	2.00	8.18	2.53	(ix)
1.434	0810.894	36.25	1.469	58.20	-4,589	-74.51	-12.84	2.12	8.11	2.55	(ix)
1.460	0810.920	34.31	1.459	56.25	-4,610	-72.28	-12.90	2.72	7.66	2.48	(xii)
1.567	0811.027	34.15	1.200	58.38	-4,621	-73.95	-12.74	2.86	8.57	2.45	(Paranal)
2.059	0811.519	–	–	–	–	-71.60	-9.01	3.34	6.20	–	(xiv)
2.360	0811.820	51.34	1.118	53.70	-4,588	-71.90	-10.68	3.82	6.21	2.92	(ix)
2.375	0811.835	50.95	1.112	53.70	-4,681	-71.02	-11.18	3.42	6.62	2.96	(ix)
2.389	0811.849	53.87	1.107	53.85	-4,728	-71.97	-10.30	3.47	6.77	3.08	(ix)
2.403	0811.863	51.45	1.103	54.05	-4,747	-72.00	-11.24	3.44	6.16	3.02	(ix)
2.409	0811.869	54.02	1.101	55.35	-4,724	-74.30	-12.17	4.48	6.17	3.08	(xii)
2.418	0811.878	51.37	1.099	54.05	-4,720	-71.12	-10.82	3.38	6.47	3.00	(ix)
2.432	0811.892	51.84	1.095	53.65	-4,704	-70.70	-9.94	3.32	6.44	3.00	(ix)
2.485	0811.945	–	–	–	–	-73.10	-11.89	4.68	6.15	–	(xv)
3.386	0812.846	56.51	0.815	50.33	-4,781	-70.76	-9.09	2.90	3.94	3.12	(Ondrejov)
3.414	0812.874	58.07	0.809	49.10	-4,547	-73.70	-10.20	2.97	4.65	2.99	(xiii)
3.449	0812.909	–	–	–	–	-73.78	-10.74	4.55	4.71	–	(xvi)
3.455	0812.915	–	–	–	–	-73.33	-9.83	4.50	3.69	–	(xv)
3.488	0812.948	56.69	0.796	48.65	-4,555	-71.12	-9.45	2.91	3.62	2.90	(xi)
3.759	0813.219	45.22	0.587	46.80	-4,599	-74.56	-10.15	3.69	–	2.41	(Paranal)
4.363	0813.823	58.43	0.636	43.40	-4,416	-70.67	-9.46	2.16	3.01	2.61	(ix)
4.369	0813.829	57.90	0.635	45.03	-4,795	-69.85	-8.18	2.01	3.07	2.58	(Ondrejov)
4.392	0813.852	55.24	0.631	44.65	-4,331	-71.65	-8.61	2.09	3.06	2.49	(ix)
4.406	0813.866	59.04	0.628	45.05	-4,352	-69.86	-9.10	1.79	2.66	2.58	(ix)
4.420	0813.880	59.43	0.626	45.05	-4,371	-70.34	-8.68	1.97	3.04	2.60	(ix)
4.424	0813.884	59.27	0.625	44.78	-4,382	-69.90	-6.19	2.30	2.41	2.60	(xi)
4.434	0813.894	57.09	0.623	44.75	-4,342	-69.47	-9.63	2.08	2.86	2.53	(ix)
4.439	0813.899	57.91	0.622	43.45	-4,400	–	–	1.87	2.95	2.58	(xiii)
4.493	0813.953	59.71	0.612	44.05	-4,450	-70.57	-8.90	3.19	3.32	2.65	(vii)
4.751	0814.211	44.77	0.461	42.78	-4,598	-72.55	-10.88	2.36	3.41	2.36	(Paranal)
5.018	0814.478	57.67	0.516	42.54	-4,355	-70.67	-10.37	2.03	2.72	2.38	(xvii)

Table 9. continued

Age ^a	Date ^b	F_{α}^c	$F_{\text{cont.}}^d$	FWHM ^e	v_{∞}^f	RV_{abs}^g	RV_{em}^g	F_{abs}^h	F_{em}^h	\dot{M}_{WD}^i	Obs. ^j
5.343	0814.803	52.50	0.457	40.88	-4,300	-67.56	-8.63	0.73	2.80	2.09	(Ondrejov)
5.378	0814.838	53.57	0.451	41.00	-4,348	-67.79	-8.41	0.98	2.97	2.06	(xii)
5.409	0814.869	55.15	0.445	40.65	-4,262	–	–	0.24	1.44	2.03	(xviii)
5.423	0814.883	52.62	0.444	41.45	-4,150	-68.36	-10.80	1.21	2.42	1.92	(ix)
5.425	0814.885	55.60	0.444	41.05	-4,343	-69.27	-8.97	0.92	2.57	2.06	(xii)
5.452	0814.912	51.07	0.441	40.55	-4,349	-70.70	-8.58	0.82	1.83	1.97	(xi)
5.759	0815.219	40.15	0.346	40.37	-4,577	-71.02	-11.63	1.34	2.49	1.74	(Paranal)
6.444	0815.904	49.39	0.351	38.45	-4,260	-72.33	-12.49	0.41	2.17	1.83	(x)
7.368	0816.828	–	–	–	–	-70.61	-10.76	0.16	1.35	–	(xvi)
7.371	0816.831	39.29	0.269	36.15	-4,172	-77.00	-11.91	0.28	1.40	1.64	(ix)
7.397	0816.857	40.26	0.269	37.35	-4,165	-71.22	-4.52	0.38	1.21	1.66	(xiii)
8.388	0817.848	40.88	0.246	33.65	-4,332	-71.67	-5.44	0.31	1.07	1.70	(xiii)
8.402	0817.862	–	–	–	–	-71.40	-11.56	0.15	1.41	–	(xvi)
9.384	0818.844	40.28	0.223	32.35	-4,175	–	–	0.17	0.81	1.59	(xiii)
9.510	0818.970	35.29	0.199	31.86	-4,563	-71.71	-9.82	0.60	0.67	1.63	(Paranal)
9.724	0819.184	–	–	–	–	-71.50	-10.73	0.10	0.77	–	(xix)
10.400	0819.860	36.69	0.200	30.15	-4,063	-72.59	-5.44	0.12	0.75	1.42	(xiii)
10.473	0819.933	–	–	–	–	-73.43	-10.85	0.10	0.80	–	(xv)
11.395	0820.855	30.94	0.182	29.20	-4,064	-73.06	-9.56	0.06	0.46	1.19	(ix)
11.431	0820.891	35.38	0.182	28.90	-4,100	-70.30	–	0.03	0.53	1.28	(xiii)
11.440	0820.900	–	–	–	–	-72.70	-10.57	–	–	–	(xv)
11.559	0821.019	30.33	0.166	28.44	-4,484	-72.11	-9.07	0.36	0.41	1.26	(Paranal)
11.711	0821.171	–	–	–	–	-69.69	-6.65	0.11	0.54	–	(xix)
12.355	0821.815	34.67	0.175	26.32	-5,425	-73.04	-7.26	0.03	0.35	1.50	(Ondrejov)
12.366	0821.826	33.87	0.174	26.32	-5,316	-75.78	-7.72	0.03	0.36	1.49	(Ondrejov)
12.456	0821.916	36.53	0.174	26.25	-4,101	-71.22	-3.61	0.04	0.51	1.48	(xiii)
13.147	0822.607	35.06	0.165	25.98	-4,275	-77.20	-5.48	0.16	0.41	1.48	(xvii)
13.467	0822.927	34.12	0.161	25.55	-4,064	-70.48	-10.64	0.00	0.46	1.36	(xiii)
14.402	0823.862	34.20	0.149	24.00	-4,075	-70.30	–	0.01	0.55	1.32	(xiii)
15.419	0824.879	26.97	0.136	23.20	-3,976	–	-7.78	0.01	0.31	1.09	(xi)
15.456	0824.916	–	–	–	–	-73.64	-10.14	0.06	0.24	–	(xv)
16.374	0825.834	28.17	0.125	22.45	-4,063	-79.61	-9.27	0.03	0.41	1.08	(ix)
16.439	0825.899	28.13	0.124	22.40	-3,933	–	-3.92	0.00	0.36	1.05	(xi)
16.448	0825.908	–	–	–	–	-72.92	-10.10	0.04	0.42	–	(xv)
17.384	0826.844	30.34	0.113	21.75	-3,951	–	–	–	0.32	1.05	(xiii)
18.431	0827.891	–	–	–	–	-72.83	-10.25	0.04	0.38	–	(xv)
18.452	0827.912	22.35	0.100	21.25	-3,937	–	-8.46	0.00	0.23	0.855	(xi)
19.356	0828.816	21.39	0.0895	20.90	-3,888	–	-7.54	0.00	0.23	0.789	(ix)
19.376	0828.836	24.01	0.0892	20.80	-4,138	–	-7.12	0.00	0.27	0.890	(xiii)
20.373	0829.833	26.94	0.0802	20.05	-4,315	–	-10.50	0.01	0.35	0.932	(xiii)
21.583	0831.043	23.47	0.0775	19.38	-4,345	-71.06	-8.48	0.12	0.29	0.851	(Paranal)
22.085	0831.545	–	–	–	–	-71.62	-7.21	0.02	0.32	–	(xiv)
22.420	0831.880	–	–	–	–	-72.16	-11.40	0.03	0.28	–	(xv)
23.347	0901.807	20.00	0.0660	17.95	-4,061	–	-2.27	0.05	0.21	0.704	(ix)
23.381	0901.841	20.33	0.0658	17.05	-3,933	–	–	–	–	0.687	(xi)
24.317	0802.777	15.97	0.0614	18.24	-4,752	–	-6.35	–	0.08	0.624	(Ondrejov)
24.386	0902.846	16.81	0.0611	18.10	-3,898	–	-4.79	–	0.26	0.616	(xi)
24.422	0902.882	–	–	–	–	-73.39	-12.64	0.02	0.27	–	(xv)
25.417	0903.877	20.44	0.0563	16.45	-4,074	–	-9.11	–	0.36	0.702	(xiii)
26.378	0904.838	21.13	0.0541	16.25	-4,386	–	-5.52	0.00	0.30	0.715	(xiii)
26.559	0905.019	15.57	0.0487	17.42	-4,272	-70.90	-8.12	0.06	0.15	0.599	(Paranal)
27.375	0905.835	18.63	0.0518	15.90	-4,301	–	-4.72	–	0.22	0.641	(xiii)
27.407	0905.867	16.10	0.0517	17.10	-4,136	–	-8.91	–	0.20	0.573	(xi)
28.394	0906.854	14.99	0.0494	15.50	-4,068	–	-4.43	–	0.15	0.533	(xi)
29.345	0907.805	14.57	0.0472	15.55	-3,956	–	–	–	–	0.503	(xx)
30.391	0908.851	17.17	0.0447	14.50	-4,071	–	-5.09	–	–	0.549	(xiii)
31.336	0909.796	13.67	0.0425	14.54	-4,589	–	-4.98	–	0.02	0.520	(Ondrejov)

Table 9. continued

Age ^a	Date ^b	F_{α}^c	$F_{\text{cont.}}^d$	FWHM ^e	v_{∞}^f	RV_{abs}^g	RV_{em}^g	F_{abs}^h	F_{em}^h	\dot{M}_{WD}^i	Obs. ^j
31.397	0909.857	14.59	0.0423	14.33	-3,929	–	–	–	–	0.481	(xx)
32.389	0910.849	12.96	0.0386	14.30	-4,064	–	-2.08	–	–	0.446	(xiii)
32.549	0911.009	11.55	0.0341	15.18	-4,299	-71.02	-4.33	0.08	0.12	0.441	(Paranal)
34.379	0912.839	11.48	0.0341	13.85	-4,040	–	–	–	–	0.417	(xiii)
35.331	0913.791	10.07	0.0334	14.19	-4,131	–	–	–	–	0.382	(xx)
35.995	0914.455	10.34	0.0329	13.95	-4,131	–	–	–	–	0.372	(xvii)
37.532	0915.992	07.24	0.0232	13.58	-4,306	-72.20	–	0.02	–	0.292	(Paranal)
38.328	0916.788	09.17	0.0311	12.57	-3,766	–	–	–	–	0.288	(xx)
38.335	0916.795	09.68	0.0311	12.89	-3,857	–	–	–	–	0.303	(xxi)
41.071	0919.531	09.79	0.0291	12.41	-4,040	–	–	–	–	0.315	(xvii)
41.390	0919.850	10.70	0.0289	12.25	-4,086	–	–	–	–	0.328	(xiii)
42.566	0921.026	08.17	0.0197	12.18	-4,040	–	–	–	–	0.283	(Paranal)
44.040	0922.500	08.23	0.0272	11.90	-4,040	–	–	–	–	–	(xvii)

Notes. ^(a) As in Table 3, ^(b) as in Table 6, ^(c) F_{α} – flux of the broad component in $10^{-9} \text{ erg s}^{-1} \text{ cm}^{-2}$, ^(d) $F_{\text{cont.}}$ – flux of the local continuum in $10^{-10} \text{ erg s}^{-1} \text{ cm}^{-2} \text{ \AA}^{-1}$, ^(e) FWHM – Full Width at Half Maximum in \AA , ^(f) v_{∞} – terminal velocity from the blue wing in km s^{-1} , ^(g) RV_{abs} and RV_{em} – radial velocities of narrow absorption and emission components in km s^{-1} , ^(h) F_{abs} and F_{em} – their fluxes in $10^{-10} \text{ erg s}^{-1} \text{ cm}^{-2}$, ⁽ⁱ⁾ \dot{M}_{WD} – mass-loss rate in $10^{-4} M_{\odot} \text{ yr}^{-1}$, ^(j) label of the observatory (Table 1, Sect. 2.2). The parameter uncertainties are described in Sects. 3.5.1, 3.5.2, and 3.3.

REFERENCES

- Abe, K., Abe, S., Abhishek, A., et al. 2025, *A&A*, 695, A152, doi: [10.1051/0004-6361/202452447](https://doi.org/10.1051/0004-6361/202452447)
- Acciari, V. A., Ansoldi, S., Antonelli, L. A., et al. 2022, *Nature Astronomy*, 6, 689, doi: [10.1038/s41550-022-01640-z](https://doi.org/10.1038/s41550-022-01640-z)
- Aydi, E., Sokolovsky, K. V., Chomiuk, L., et al. 2020, *Nature Astronomy*, 4, 776, doi: [10.1038/s41550-020-1070-y](https://doi.org/10.1038/s41550-020-1070-y)
- Azzollini, A., Shore, S. N., Kuin, P., & Page, K. L. 2023, *A&A*, 674, A139, doi: [10.1051/0004-6361/202245185](https://doi.org/10.1051/0004-6361/202245185)
- Banerjee, D. P. K., Das, R. K., & Ashok, N. M. 2009, *MNRAS*, 399, 357, doi: [10.1111/j.1365-2966.2009.15279.x](https://doi.org/10.1111/j.1365-2966.2009.15279.x)
- Barry, R. K., Danchi, W. C., Traub, W. A., et al. 2008, *ApJ*, 677, 1253, doi: [10.1086/529422](https://doi.org/10.1086/529422)
- Bermúdez-Bustamante, L. C., García-Segura, G., Steffen, W., & Sabin, L. 2020, *MNRAS*, 493, 2606, doi: [10.1093/mnras/staa403](https://doi.org/10.1093/mnras/staa403)
- Bessell, M. S. 1979, *PASP*, 91, 589, doi: [10.1086/130542](https://doi.org/10.1086/130542)
- Bjorkman, J. E., & Cassinelli, J. P. 1993, *ApJ*, 409, 429, doi: [10.1086/172676](https://doi.org/10.1086/172676)
- Bode, M. F., & Evans, A. 2008, *Classical Novae*, Vol. 43 (Cambridge University Press: Cambridge)
- Bode, M. F., Harman, D. J., O'Brien, T. J., et al. 2007, *ApJL*, 665, L63, doi: [10.1086/520929](https://doi.org/10.1086/520929)
- Bohm, D., & Aller, L. H. 1947, *ApJ*, 105, 131, doi: [10.1086/144890](https://doi.org/10.1086/144890)
- Booth, R. A., Mohamed, S., & Podsiadlowski, P. 2016, *MNRAS*, 457, 822, doi: [10.1093/mnras/stw001](https://doi.org/10.1093/mnras/stw001)
- Brandi, E., Quiroga, C., Mikołajewska, J., Ferrer, O. E., & García, L. G. 2009, *A&A*, 497, 815, doi: [10.1051/0004-6361/200811417](https://doi.org/10.1051/0004-6361/200811417)
- Cardelli, J. A., Clayton, G. C., & Mathis, J. S. 1989, *ApJ*, 345, 245, doi: [10.1086/167900](https://doi.org/10.1086/167900)
- Cariková, Z., & Skopal, A. 2012, *A&A*, 548, A21, doi: [10.1051/0004-6361/201219221](https://doi.org/10.1051/0004-6361/201219221)
- Chesneau, O., Nardetto, N., Millour, F., et al. 2007, *A&A*, 464, 119, doi: [10.1051/0004-6361:20066609](https://doi.org/10.1051/0004-6361:20066609)
- Cheung, C. C., Johnson, T. J., Jean, P., et al. 2022, *ApJ*, 935, 44, doi: [10.3847/1538-4357/ac7eb7](https://doi.org/10.3847/1538-4357/ac7eb7)
- Chomiuk, L., Metzger, B. D., & Shen, K. J. 2021, *ARA&A*, 59, 391, doi: [10.1146/annurev-astro-112420-114502](https://doi.org/10.1146/annurev-astro-112420-114502)
- Chomiuk, L., Linford, J. D., Yang, J., et al. 2014, *Nature*, 514, 339, doi: [10.1038/nature13773](https://doi.org/10.1038/nature13773)
- de Ruiter, I., Nyamai, M. M., Rowlinson, A., et al. 2023, *MNRAS*, 523, 132, doi: [10.1093/mnras/stad1418](https://doi.org/10.1093/mnras/stad1418)
- De Sarkar, A., Nayana, A. J., Roy, N., Razzaque, S., & Anupama, G. C. 2023, *ApJ*, 951, 62, doi: [10.3847/1538-4357/acd6ed](https://doi.org/10.3847/1538-4357/acd6ed)
- Dekker, H., D'Odorico, S., Kaufer, A., Delabre, B., & Kotzlowski, H. 2000, in *Society of Photo-Optical Instrumentation Engineers (SPIE) Conference Series*, Vol. 4008, *Optical and IR Telescope Instrumentation and Detectors*, ed. M. Iye & A. F. Moorwood, 534–545, doi: [10.1117/12.395512](https://doi.org/10.1117/12.395512)
- Diesing, R., Metzger, B. D., Aydi, E., et al. 2023, *ApJ*, 947, 70, doi: [10.3847/1538-4357/acc105](https://doi.org/10.3847/1538-4357/acc105)
- Evans, A., Callus, C. M., Albinson, J. S., et al. 1988, *MNRAS*, 234, 755, doi: [10.1093/mnras/234.3.755](https://doi.org/10.1093/mnras/234.3.755)
- Gurzadyan, G. A. 1997, *The Physics and Dynamics of Planetary Nebulae*
- H. E. S. S. Collaboration, Aharonian, F., Ait Benkhali, F., et al. 2022, *Science*, 376, 77, doi: [10.1126/science.abn0567](https://doi.org/10.1126/science.abn0567)
- Hachisu, I., & Kato, M. 2010, *ApJ*, 709, 680, doi: [10.1088/0004-637X/709/2/680](https://doi.org/10.1088/0004-637X/709/2/680)
- Healy-Kalesh, M. W., Darnley, M. J., Harvey, É. J., & Newsam, A. M. 2024, *MNRAS*, 529, L175, doi: [10.1093/mnras/slac016](https://doi.org/10.1093/mnras/slac016)
- Henden, A. A., & Kaitchuck, R. H. 1982, *Astronomical photometry*
- Hjellming, R. M., van Gorkom, J. H., Taylor, A. R., et al. 1986, *ApJL*, 305, L71, doi: [10.1086/184687](https://doi.org/10.1086/184687)
- Islam, N., Mukai, K., & Sokoloski, J. L. 2024, *ApJ*, 960, 125, doi: [10.3847/1538-4357/ad1041](https://doi.org/10.3847/1538-4357/ad1041)
- Kato, M., & Hachisu, I. 1994, *Astrophys. J.*, 437, 802, doi: [10.1086/175041](https://doi.org/10.1086/175041)
- Kato, M., Saio, H., & Hachisu, I. 2022, *ApJL*, 935, L15, doi: [10.3847/2041-8213/ac85c1](https://doi.org/10.3847/2041-8213/ac85c1)
- Kato, M., Saio, H., Henze, M., et al. 2016, *ApJ*, 830, 40, doi: [10.3847/0004-637X/830/1/40](https://doi.org/10.3847/0004-637X/830/1/40)
- Kudzej, I., & Dubovský, P. 2014, *Contributions of the Astronomical Observatory Skalnaté Pleso*, 43, 429
- Lamers, H. J. G. L. M., & Cassinelli, J. P. 1999, *Introduction to Stellar Winds*
- Leitherer, C. 1988, *ApJ*, 326, 356, doi: [10.1086/166097](https://doi.org/10.1086/166097)
- Li, K.-L., Metzger, B. D., Chomiuk, L., et al. 2017, *Nature Astronomy*, 1, 697, doi: [10.1038/s41550-017-0222-1](https://doi.org/10.1038/s41550-017-0222-1)
- Lico, R., Giroletti, M., Munari, U., et al. 2024, *A&A*, 692, A107, doi: [10.1051/0004-6361/202451364](https://doi.org/10.1051/0004-6361/202451364)
- Livio, M., Shankar, A., Burkert, A., & Truran, J. W. 1990, *ApJ*, 356, 250, doi: [10.1086/168836](https://doi.org/10.1086/168836)
- Lloyd, H. M., O'Brien, T. J., & Bode, M. F. 1997, *MNRAS*, 284, 137, doi: [10.1093/mnras/284.1.137](https://doi.org/10.1093/mnras/284.1.137)
- Luna, G. J. M., Montez, R., Sokoloski, J. L., Mukai, K., & Kastner, J. H. 2009, *ApJ*, 707, 1168, doi: [10.1088/0004-637X/707/2/1168](https://doi.org/10.1088/0004-637X/707/2/1168)
- Martin, P., & Dubus, G. 2013, *A&A*, 551, A37, doi: [10.1051/0004-6361/201220289](https://doi.org/10.1051/0004-6361/201220289)

- Martin, P., Dubus, G., Jean, P., Tatischeff, V., & Dosne, C. 2018, *A&A*, 612, A38, doi: [10.1051/0004-6361/201731692](https://doi.org/10.1051/0004-6361/201731692)
- Metzger, B. D., Finzell, T., Vurm, I., et al. 2015, *MNRAS*, 450, 2739, doi: [10.1093/mnras/stv742](https://doi.org/10.1093/mnras/stv742)
- Metzger, B. D., Hascoët, R., Vurm, I., et al. 2014, *MNRAS*, 442, 713, doi: [10.1093/mnras/stu844](https://doi.org/10.1093/mnras/stu844)
- Molaro, P., Izzo, L., Selvelli, P., et al. 2023, *MNRAS*, 518, 2614, doi: [10.1093/mnras/stac2708](https://doi.org/10.1093/mnras/stac2708)
- Montez, R., Luna, G. J. M., Mukai, K., Sokoloski, J. L., & Kastner, J. H. 2022, *ApJ*, 926, 100, doi: [10.3847/1538-4357/ac4583](https://doi.org/10.3847/1538-4357/ac4583)
- Morrison, W. 1985, *IAUC*, 4030, 2
- Munari, U. 2019, arXiv e-prints, arXiv:1909.01389, doi: [10.48550/arXiv.1909.01389](https://doi.org/10.48550/arXiv.1909.01389)
- . 2025, *Contributions of the Astronomical Observatory Skalnaté Pleso*, 55, 47, doi: [10.31577/caosp.2025.55.3.47](https://doi.org/10.31577/caosp.2025.55.3.47)
- Munari, U., Giroletti, M., Marcote, B., et al. 2022, *A&A*, 666, L6, doi: [10.1051/0004-6361/202244821](https://doi.org/10.1051/0004-6361/202244821)
- Munari, U., Sordo, R., Castelli, F., & Zwitter, T. 2005, *A&A*, 442, 1127, doi: [10.1051/0004-6361:20042490](https://doi.org/10.1051/0004-6361:20042490)
- Munari, U., & Valisa, P. 2021, arXiv e-prints, arXiv:2109.01101, doi: [10.48550/arXiv.2109.01101](https://doi.org/10.48550/arXiv.2109.01101)
- . 2022, arXiv e-prints, arXiv:2203.01378, doi: [10.48550/arXiv.2203.01378](https://doi.org/10.48550/arXiv.2203.01378)
- Mürset, U., & Schmid, H. M. 1999, *A&AS*, 137, 473, doi: [10.1051/aas:1999105](https://doi.org/10.1051/aas:1999105)
- Narumi, H., Hirosawa, K., Kanai, K., et al. 2006, *IAUC*, 8671, 2
- Nauenberg, M. 1972, *ApJ*, 175, 417, doi: [10.1086/151568](https://doi.org/10.1086/151568)
- Ness, J., Starrfield, S., Page, K. L., et al. 2007, *Progress of Theoretical Physics Supplement*, 169, 187, doi: [10.1143/PTPS.169.187](https://doi.org/10.1143/PTPS.169.187)
- Ness, J. U., Beardmore, A. P., Bode, M. F., et al. 2023, *A&A*, 670, A131, doi: [10.1051/0004-6361/202245269](https://doi.org/10.1051/0004-6361/202245269)
- Nikolov, Y., Luna, G. J. M., Stoyanov, K. A., et al. 2023, *A&A*, 679, A150, doi: [10.1051/0004-6361/202346997](https://doi.org/10.1051/0004-6361/202346997)
- Nussbaumer, H., & Vogel, M. 1987, *A&A*, 182, 51
- O'Brien, T. J., Bode, M. F., Porcas, R. W., et al. 2006, *Nature*, 442, 279, doi: [10.1038/nature04949](https://doi.org/10.1038/nature04949)
- Orio, M., Gendreau, K., Giese, M., et al. 2023, *ApJ*, 955, 37, doi: [10.3847/1538-4357/ace9bd](https://doi.org/10.3847/1538-4357/ace9bd)
- Osterbrock, D. E. 1989, *Astrophysics of gaseous nebulae and active galactic nuclei*
- Page, K. L., Beardmore, A. P., Osborne, J. P., et al. 2022, *MNRAS*, 514, 1557, doi: [10.1093/mnras/stac1295](https://doi.org/10.1093/mnras/stac1295)
- Pandey, R., Srivastava, M. K., Maiti, A., et al. 2025, *MNRAS*, 540, 3549, doi: [10.1093/mnras/staf933](https://doi.org/10.1093/mnras/staf933)
- Parimucha, Š., & Vaňko, M. 2005, *Contributions of the Astronomical Observatory Skalnaté Pleso*, 35, 35
- Pavlenko, Y. V., Evans, A., Kerr, T., et al. 2008, *A&A*, 485, 541, doi: [10.1051/0004-6361:20078622](https://doi.org/10.1051/0004-6361:20078622)
- Ribeiro, V. A. R. M., Munari, U., & Valisa, P. 2013, *ApJ*, 768, 49, doi: [10.1088/0004-637X/768/1/49](https://doi.org/10.1088/0004-637X/768/1/49)
- Rosino, L. 1987, in *RS Ophiuchi (1985) and the Recurrent Nova Phenomenon*, ed. M. F. Bode, 1
- Rupen, M. P., Mioduszewski, A. J., & Sokoloski, J. L. 2008, *ApJ*, 688, 559, doi: [10.1086/525555](https://doi.org/10.1086/525555)
- Schaefer, B. E. 2010, *ApJS*, 187, 275, doi: [10.1088/0067-0049/187/2/275](https://doi.org/10.1088/0067-0049/187/2/275)
- Schaefer, G. H., Brummelaar, T. T., Gies, D. R., et al. 2014, *Nature*, 515, 234, doi: [10.1038/nature13834](https://doi.org/10.1038/nature13834)
- Sekeráš, M., Skopal, A., Shugarov, S., et al. 2019, *Contributions of the Astronomical Observatory Skalnaté Pleso*, 49, 19. <https://arxiv.org/abs/1904.05555>
- Shagatova, N., Skopal, A., & Cariková, Z. 2016, *A&A*, 588, A83, doi: [10.1051/0004-6361/201525645](https://doi.org/10.1051/0004-6361/201525645)
- Skoda, P., Slechta, M., & Honsa, J. 2002, *Publications of the Astronomical Institute of the Czech Academy of Sciences*, 90
- Skopal, A. 2005, *A&A*, 440, 995, doi: [10.1051/0004-6361:20034262](https://doi.org/10.1051/0004-6361:20034262)
- . 2006, *A&A*, 457, 1003, doi: [10.1051/0004-6361:20064935](https://doi.org/10.1051/0004-6361:20064935)
- . 2007, *NewA*, 12, 597, doi: [10.1016/j.newast.2007.04.003](https://doi.org/10.1016/j.newast.2007.04.003)
- . 2015, *NewA*, 36, 128, doi: [10.1016/j.newast.2013.12.005](https://doi.org/10.1016/j.newast.2013.12.005)
- . 2019, *ApJ*, 878, 28, doi: [10.3847/1538-4357/ab1f07](https://doi.org/10.3847/1538-4357/ab1f07)
- Skopal, A., Pribulla, T., Buil, C., Vittone, A., & Errico, L. 2008, in *Astronomical Society of the Pacific Conference Series*, Vol. 401, *RS Ophiuchi (2006) and the Recurrent Nova Phenomenon*, ed. A. Evans, M. F. Bode, T. J. O'Brien, & M. J. Darnley, 227, doi: [10.48550/arXiv.0802.3711](https://doi.org/10.48550/arXiv.0802.3711)
- Skopal, A., & Shagatova, N. 2023, *A&A*, 680, A60, doi: [10.1051/0004-6361/202347396](https://doi.org/10.1051/0004-6361/202347396)
- Skopal, A., Vittone, A. A., Errico, L., et al. 2006, *A&A*, 453, 279, doi: [10.1051/0004-6361:20052917](https://doi.org/10.1051/0004-6361:20052917)
- Skopal, A., Drechsel, H., Tarasova, T., et al. 2014, *A&A*, 569, A112, doi: [10.1051/0004-6361/201424284](https://doi.org/10.1051/0004-6361/201424284)
- Skopal, A., Shugarov, S. Y., Sekeráš, M., et al. 2017, *A&A*, 604, A48, doi: [10.1051/0004-6361/201629593](https://doi.org/10.1051/0004-6361/201629593)
- Skopal, A., Shugarov, S. Y., Munari, U., et al. 2020, *A&A*, 636, A77, doi: [10.1051/0004-6361/201937199](https://doi.org/10.1051/0004-6361/201937199)
- Starrfield, S., Iliadis, C., & Hix, W. R. 2016, *PASP*, 128, 051001, doi: [10.1088/1538-3873/128/963/051001](https://doi.org/10.1088/1538-3873/128/963/051001)
- Taguchi, K., Ueta, T., & Isogai, K. 2021, *The Astronomer's Telegram*, 14838, 1
- Taylor, A. R., Davis, R. J., Porcas, R. W., & Bode, M. F. 1989, *MNRAS*, 237, 81, doi: [10.1093/mnras/237.1.81](https://doi.org/10.1093/mnras/237.1.81)
- Teyssier, F. 2019, *Contributions of the Astronomical Observatory Skalnaté Pleso*, 49, 217

- Tomov, N. A., Tomova, M. T., Stoyanov, K. A., et al. 2023, *A&A*, 671, A49, doi: [10.1051/0004-6361/202243068](https://doi.org/10.1051/0004-6361/202243068)
- Warner, B. 2008, in *Classical Novae*, ed. M. F. Bode & A. Evans, Vol. 43, 16–33, doi: [10.1017/CBO9780511536168.004](https://doi.org/10.1017/CBO9780511536168.004)
- West, J. D. 2006, *IAUC*, 8683, 3
- Yaron, O., Prialnik, D., Shara, M. M., & Kovetz, A. 2005, *ApJ*, 623, 398, doi: [10.1086/428435](https://doi.org/10.1086/428435)
- Zamanov, R. K., Stoyanov, K. A., Nikolov, Y. M., et al. 2022, *Bulgarian Astronomical Journal*, 37, 24, doi: [10.48550/arXiv.2109.11306](https://doi.org/10.48550/arXiv.2109.11306)
- Zamanov, R. K., Boeva, S., Latev, G. Y., et al. 2018, *MNRAS*, 480, 1363, doi: [10.1093/mnras/sty1816](https://doi.org/10.1093/mnras/sty1816)
- Zheng, J.-H., Huang, Y.-Y., Zhang, Z.-L., et al. 2022, *PhRvD*, 106, 103011, doi: [10.1103/PhysRevD.106.103011](https://doi.org/10.1103/PhysRevD.106.103011)